AD-A129 561 WATER WAVE SLOPE ESTIMATION(U) SYSTEMS CONTROL 1/1
TECHNOLOGY INC PALO ALTO CA K S KRISHNAN ET AL. FEB 82
N00014-81-C-0357

UNCLASSIFIED F/G 8/10 NL

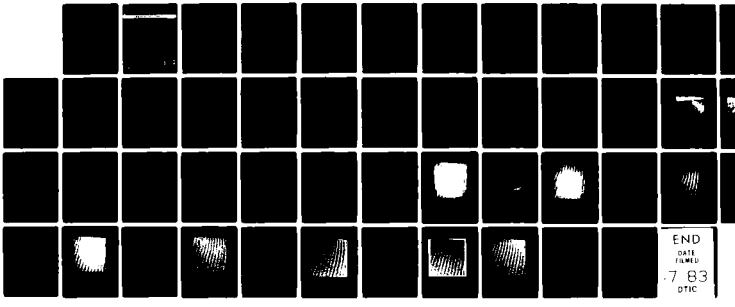

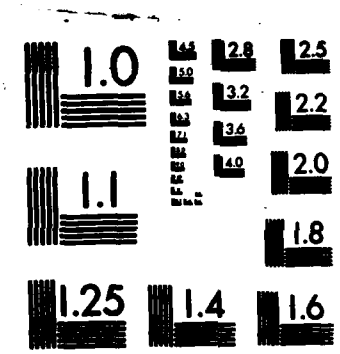

(2)

SCT SYSTEMS CONTROL TECHNOLOGY, INC.
1801 PAGE MILL RD. □ P.O. BOX 10150 □ PALO ALTO, CALIFORNIA 94303 □ (415) 494-2233

FINAL REPORT

WATER WAVE SLOPE ESTIMATION

Contract No. N00014-81-C-0357

FEBRUARY 1982

Submitted to:

Scientific Officer
Office of Naval Research
Department of the Navy
800 North Quincy Street
Arlington, VA 22217
Attn: Dr. James S. Bailey

Prepared by:

K. S. Krishnan

R. G. Ollenburger

TABLE OF CONTENTS

LIST OF FIGURES

LIST OF TABLES

Tables

ACKNOWLEDGEMENT

During the development of the technique over the past several years, a number of colleagues and coworkers have provided a variety of assistance. The contributions of Drs. J. R. Jain, R. S. Poulsen, M. A. Nokes and Mrs. U. B. Shah, members of the staff of Systems Control, Inc. and Systems Control Technology, Inc., are appreciated. The initial development by the technique was partially supported by Applied Physics Labratory. The Johns Hopkins Univesity, Laurel, MD. under Subcontract No. 600711 of Contract N0001~~4~~-72-C-1101. The cameras used for the work reported herein were loaned to us by APL/JHU, through the courtesies of Dr. R. Gasparovic. Finally, we thank Drs. Ming-Su and P. Smith of NORDA for their help and cooperation during the experiments at the outdoor wave basin at NORDA. The work reported here was supported by the Coastal Sciences Program of the Office of Naval Research under Contract N0001~~4~~-C-81-0357.

1. INTRODUCTION

The statistical description of the geometrical features of the ocean surface such as the elevation and the slope is needed in many diverse areas of application and has been the goal of many investigations. Aside from the basic interest of physical oceanographers, the interest in these features has been stimulated by the need for remote sensing of large areas of the ocean from satellites with various sensors including synthetic aperture radar. Understanding of electromagnetic scattering by the ocean surface is necessary for this purpose. While theories abound, one of the most elusive ingredients in a complete understanding of the problem, has been the geometry of the surface, as given by the spatial distribution of the slopes over a sizeable area of the ocean surface.

Typically, experimental measurements have been of two kinds: (a) statistical results representative of a large area and (b) a time series of measurements at a point. The work of Cox and Munk [1] and Stilwell [2] represent the first kind and the anthology composed by Pierson and Stacy [3] is dominated by measurements of the second kind where probes such as wire arrays or a laser beam measure the local elevation or slope as a function of time. Except for the work reported by Cote, et al. [4] and Dobson [5] on stereo observations of waves, no measurements of the instantaneous surface geometry over a two-dimensional area have been reported. Our own interest arose during a detailed analysis of the ability of the Stilwell method to measure the directional power spectra of ocean waves. [6] Under certain conditions of observation geometry and illumination conditions, an optical image of the ocean surface can be interpreted to obtain a good approximation of the local surface slope components along the look azimuth. If such a computation could be extended to the slope component normal to the look direction and to more general and real illumination conditions, a powerful technique for measuring the ocean surface geometry would result.

A novel technique for reconstructing the slopes of the water surface using three simultaneous images of the surface obtained with polarizers oriented at three different angles, has been proposed by Krishnan [7]. An extended source of illumination such as daylight is necessary. The method

relies on the difference between the reflectances of the components of light polarized in the plane of reflection and perpendicular to the plane of reflection. Being functions of the angle of incidence, the reflectances can be used to compute the plane and angle of incidence and the slope of the surface. It must be recognized that in the measurement of a random process such as the ocean surface geometry, the only feasible check on the results is a comparison of the statistical parameters with the results of other measurements or through an appeal to theoretical arguments. However, this new method has the unique characteristic that a detailed check of the slope measurements of each sample of the random process is feasible. This paper describes the concept and the results of its application in a relatively controlled environment.

The basic theory related to the concept and the assumptions and limitations of the method are described in Section 2. Section 3 describes the experiments that were conducted at the NORDA test facility and subsequent film processing. Section 4 describes the details of the data processing and Section 5 shows example images of the data collected and the analysis results.

2. WAVE SLOPE RECONSTRUCTION TECHNIQUE

2.1 THEORETICAL FOUNDATION

The geometry specified in Figure 2-1, describes reflection at a small area of the water's surface with the unit normal $\hat{n}$ with zenith angle μ and azimuth ν . The angle of incidence (or reflection) is ω , and the reflected ray $\hat{r}$ is described by the azimuth α and nadir angle β . The plane of reflection at each point on the surface is defined by the reflected ray and the local surface normal $\hat{n}$. As shown in Figure 2-2, the trace of the plane of reflection in the plane normal to the reflected ray (or the camera aperture plane) forms an angle ϕ with the trace of the horizontal plane, and ϕ is determined by

$$\cos \phi = \frac{-\sin\mu \sin(\nu-\alpha)}{\sin \omega} \tag{2.1}$$

The angle of incidence ω given by

$$\cos \omega = -\sin\mu \sin\beta \cos(\nu-\alpha) + \cos\mu \cos\beta \ . \tag{2.2}$$

The basic idea is to determine at each location on the surface the angle of incidence from the magnitude of the reflected intensity and the plane of reflection from the polarization properties of the light reflected from that location. That these in turn determine the local surface normal and the direction of the incident ray at that location can be demonstrated by reference to Figure 2-3. The angle of incidence defines a cone of half angle ω about the (known) direction $\hat{r}$ of the reflected ray upon which surface normal $\hat{n}$ must lie. Since the incident and reflected rays and the surface normal must all lie in the plane of reflection, $\hat{n}$ must be along one of the two lines of intersection of this plane with the cone, and the associated direction of the incident ray follows immediately from the laws of reflection. The more probable direction for the surface normal is assumed to be the one lying closest to the vertical.

The manner in which the angle ω and the plane of reflection (or ϕ) are to be determined will now be demonstrated. Let the sky radiance with

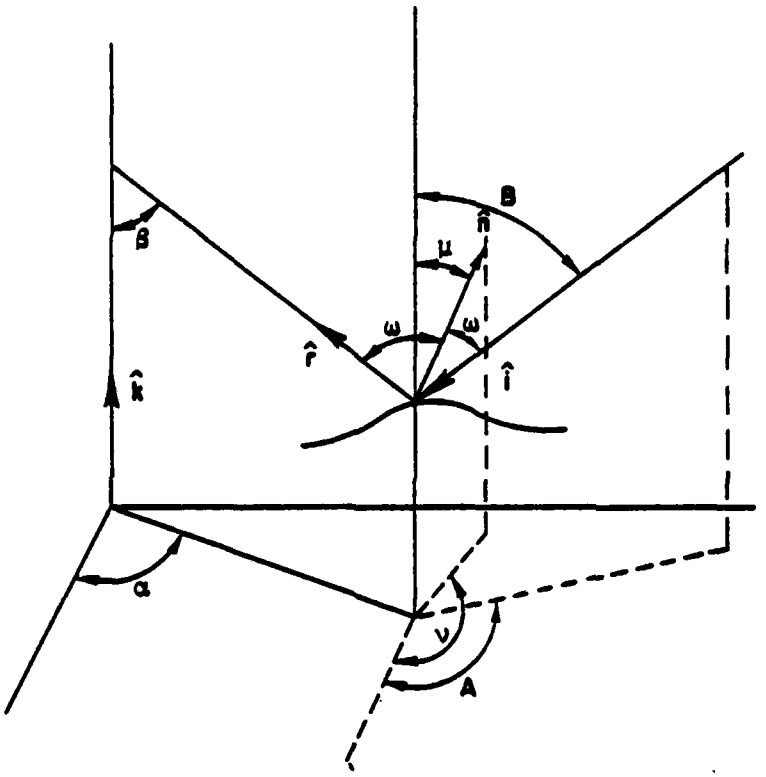

Figure 2-1 Geometry of Reflection at a Point on the Surface of Water

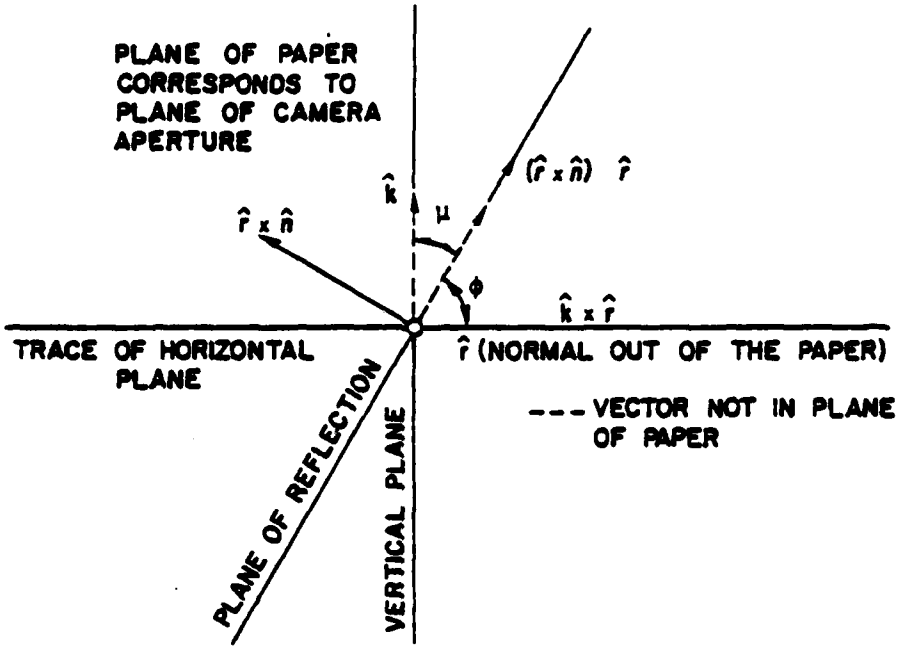

Figure 2-2 Orientation of the Plane of Reflection with Respect to the Horizontal

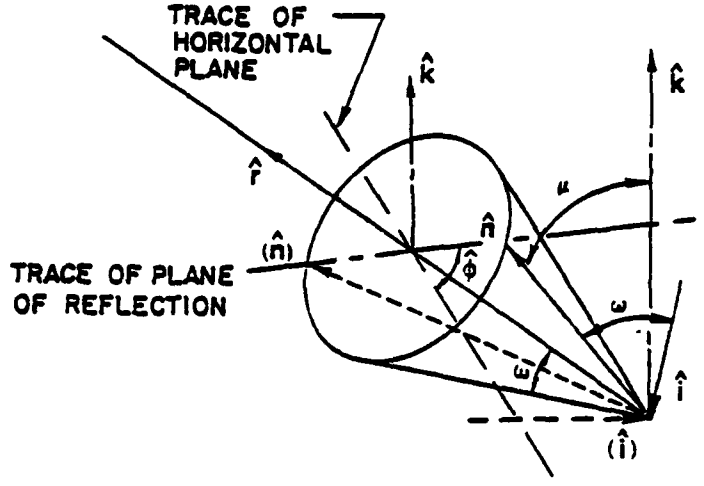

Figure 2-3 Determination of Surface Normal from Angle of Incidence and the Orientation of the Plane of Reflection. (The two possible incident rays $\hat{i}$ and $(\hat{i})$, along with their associated surface normals $\hat{n}$ and $(\hat{n})$, respectively, lie in the plane of reflection and give the same reflected ray $\hat{r}$.)

horizontal polarization be denoted by $N_h(A,B)$, and that with orthogonal polarization by $N_o(A,B)$, where A is the azimuth and B is the nadir angle of the incident ray (see Figure 2-1). It can be shown that the plane of reflection forms an angle ϕ with the horizontal in the plane normal to the incident ray, where

$$\cos \phi = \cos \phi \frac{\sin\beta}{\sin B} \tag{2.3}$$

Thus, the sky radiance incident on the surface element has parallel (p-) component

$$N_p(A,B) = N_h(A,B)\cos^2\phi + N_o(A,B)\sin^2\phi \tag{2.4}$$

and perpendicular (s-) component

$$N_s(A,B) = N_h(A,B)\sin^2\phi + N_o(A,B)\cos^2\phi \ . \tag{2.5}$$

If η_p and η_s are the reflectances of water for the p- and s-components, respectively, the irradiance at the image location corresponding to that surface element will be

$$H_t(\alpha,\beta) = \frac{\pi}{4F^2} [N_p\eta_p + N_s\eta_s] \tag{2.6}$$

where F is the f-number of the imaging system, and subscript t denotes the total irradiance (i.e., with no polarizer).

If a polarizer oriented at angle γ with respect to the horizontal is used in front of the lens, the image irradiance will be

$$\begin{aligned} H_\gamma(\alpha,\beta) = \frac{\pi}{4F^2} \{ & t_p[N_p\eta_p\cos^2(\gamma-\phi) + N_s\eta_s\sin^2(\gamma-\phi)] \\ & + t_s[N_p\eta_p\sin^2(\gamma-\phi) + N_s\eta_s\cos^2(\gamma-\phi)]\}, \end{aligned} \tag{2.7}$$

where, t_p and t_s are the transmittances of the polarization analyzer parallel and perpendicuar to its pass direction, respectively.

If three simultaneous images of the surface of water were recorded from

the same camera location with the polarizer pass directions oriented in the horizontal direction (h), the orthogonal (o) direction and at 45° to the horizontal, the respective image irradiances will be

$$H_h(\alpha,\beta) = \frac{\pi}{4F^2}\{t_p[N_p\eta_p\cos^2\phi + N_s\eta_s\sin^2\phi\} + t_s[N_p\eta_p\sin^2\phi + N_s\eta_s\cos^2\phi]\} \tag{2.8}$$

$$H_o(\alpha,\beta) = \frac{\pi}{4F^2}\{t_p[N_p\eta_p\sin^2\phi + N_s\eta_s\sin^2\phi] + t_s\{N_p\eta_p\cos^2\phi + N_s\eta_s\sin^2\phi]\} \tag{2.9}$$

$$H_{45}(\alpha,\beta) = \frac{\pi}{8F^2}\{t_p[N_p\eta_p(1+\sin 2\phi) + N_s\eta_s(1-\sin 2\phi)] + t_s[N_p\eta_p(1-\sin 2\phi) + N_s\eta_s(1+\sin 2\phi)]\} \tag{2.10}$$

from which it follows that

$$H_h + H_o = \frac{\pi}{4F^2}(t_p + t_s)(N_p\eta_p + N_s\eta_s) \tag{2.11}$$

$$H_h - H_o = \frac{\pi}{4F^2}(t_p - t_s)(N_p\eta_p - N_s\eta_s)\cos 2\phi \tag{2.12}$$

and

$$H_{45} = \frac{\pi}{8F^2}\{(t_p + t_s)(N_p\eta_p + N_s\eta_s) + (t_p - t_s)(N_p\eta_p - N_s\eta_s)\sin 2\phi].$$

$$= \frac{1}{2}\{H_h + H_o + (H_h - H_o)\tan 2\phi], \tag{2.13}$$

Therefore, the knowledge of H_h, H_o, and H_{45} determines tan 2ϕ and Equation (2.13) can be rearranged to give $\hat{\phi}$, an estimate of ϕ, by

$$\hat{\phi} = \frac{1}{2}\arctan\frac{H_o + H_h - 2H_{45}}{H_o - H_h}. \tag{2.14}$$

The angle of incidence ω must now be estimated to complete the solution. We use the known functional relationships between ω and reflectances η_s and η_p, shown in Figure 2-4, to compute ω.

The reflectance component η_s can be found by eliminating $N_p\eta_p$ from Equations (2.11) and (2.12):

$$\eta_s = \frac{2F^2}{\pi(t_p^2-t_s^2)N_s\cos 2\phi}\{H_o[(t_p-t_s)\cos 2\phi + t_p + t_s]$$

$$+H_h[(t_p-t_s)\cos 2\phi - t_p - t_s]\} \qquad (2.15)$$

Note that knowledge of the sky radiance component N_s in the direction of the incident ray is necessary for solutions of this equation. However, the direction of the incident ray cannot be calculated until the surface normal [or (μ,ν)], has been calculated, which is the final object of the reconstruction technique. An iterative solution with initial conditions (μ=0, ν=0) may be used to overcome the above difficulty. The convergence of such an iterative technique is not always guaranteed. We note that for uniform and/or unpolarized skies (which does not exist in practice) the above problem does not arise.

An alternative method of computing ω is as follows: A relationship analogous to Equation (2.15) can be derived as

$$\eta_p = \frac{2F^2}{\pi(t_p^2-t_s^2)N_p \cos 2\phi}\{H_h[(t_p - t_s)\cos 2\phi + t_p + t_s]$$

$$+ H_o[(t_p - t_s)\cos 2\phi - t_p - t_s]\} \; . \qquad (2.16)$$

The ratio of the two reflectances η_p and η_s is thus given by

$$r_\eta \triangleq \frac{\eta_p}{\eta_s} = \frac{(H_h+H_o)(t_p-t_s)\cos 2\phi - (H_o-H_h)(t_p+t_s)}{(H_h+H_o)(t_p-t_s)\cos 2\phi + (H_o-H_h)(t_p+t_s)} \cdot \frac{N_s}{N_p} \; . \qquad (2.17)$$

For unpolarized skies,

$$N_p = N_s \quad \text{or} \quad \frac{N_s}{N_p} = 1 \; , \qquad (2.18)$$

and the ratio r_η is independent of the actual value of the sky radiance.

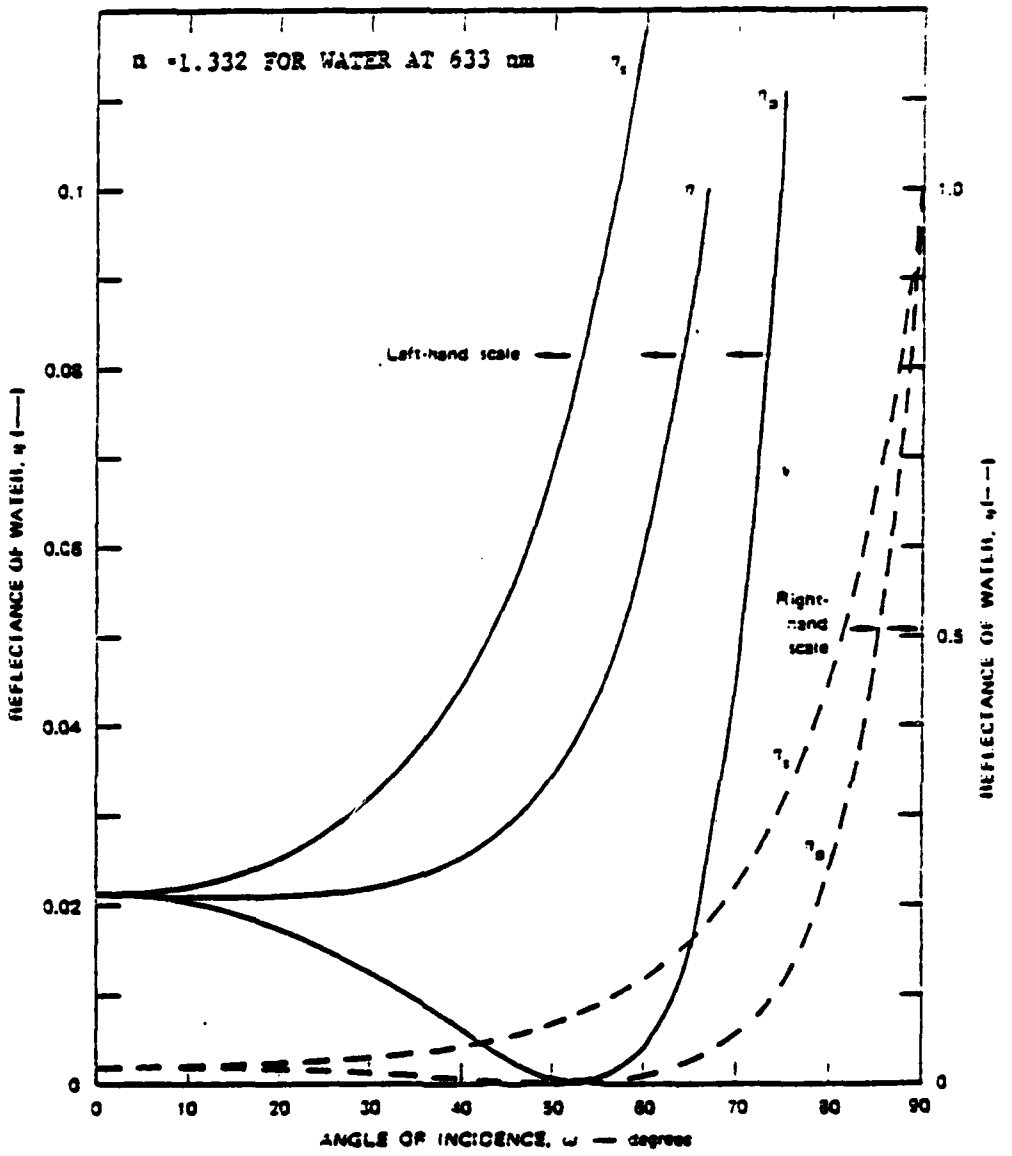

Figure 2-4 Reflectance of Water for Different Polarization

Once r_η been computed, the known functional relationship between ω and $r_\eta(\omega)$ can be used to find ω , although not unambiguously. Figure 2-5 shows this relationship. We note that each value of r_η corresponds to two values of ω , one greater than the Brewster's angle ω_c and one less than ω_c . Although this ambiguity cannot be resolved completely by the available measurements, it can be eliminated with a great degree of confidence by the choice of appropriate camera geometry. In the camera geometry employed in our experiments (nadir angle of the optic axis = 27°), ω is expected to be less than $\omega_c(\tilde{\sim} 53^0)$ in almost all the cases. Therefore, we choose only that value of ω which is less than ω_c .

Once ω and ϕ have been determined, the surface slope can be found as follows. Since ω and ϕ are the polar angle and azimuth, respectively, of the surface normal in a spherical polar coordinate system with the reflected ray forming the polar axis, μ and ν can be determined by the proper transformation of coordinates and are given by

$$\mu = \arccos(\sin\omega \sin\phi \sin\beta + \cos\omega \cos\beta) \tag{2.19}$$

$$\nu = \alpha + \text{ATAN2}\ \{-\sin\omega \cos\phi,\ (\sin\omega \cos\phi \cos\beta - \cos\omega \sin\beta)\} \ . \tag{2.20}$$

This completes the derivation of the surface slope from the three polarized irradiances.

If the surface slope tilt and azimuth were known at a given location, it is clear that the reflected irradiance can be computed for a general geometry and any polarizer pass direction. A comparison of the computed image and an actual image with a polarizer pass direction at say -45° would then be a direct check on the accuracy of the reconstructed slopes.

2.2 FEASIBILITY AND LIMITATIONS OF THE TECHNIQUE

We now consider the questions related to the experimental feasiblity and the limitations of the technique when applied to the determination of the slope of water waves. Some of these are intrinsic to the procedure, some are imposed by the methods used for processing the data and others arise from the

characteristics of the water.

We have already seen that for uniform and/or unpolarized skies, the analysis is more direct than in the more general case of nonuniform polarized skies where an iterative method may be necessary for solution. While uniform sky radiance may be uncommon, unpolarized (but nonuniform) sky radiance is common especially when the sky is hazy or overcast. Even under relatively clear conditions, substantial parts of the sky are unpolarized and may be useful. The ambiguity in ω represented by Figure 2-5 and the observation that the slopes of water waves rarely exceed 0.5 (corresponding to a tilt angle μ = 26.6°) , suggest the use of a bias angle of 27°, approximately one-half the Brewsters' angle for water. Orienting the optic axis of the imaging system at a nadir angle of 27°, limits the reflectance of water to low values, reducing the total amount of reflected light available and the contrast in the images. These conditions will be particularly poor for the p-polarized component from those slopes which are tilted at 27° from the vertical away from the optic axis. (Note that the corresponding incident ray must be almost horizontal.) Further, for those slopes tilted near 27° from the vertical toward the optic axis, the difference between the polarizations disappears because for such slopes no unique plane of reflection exists as is also evident from the ambiguity in the value of ϕ from Equation (2.20) and Figure 2-3. For a given level of noise, the errors in reconstruction will therefore be large for slopes with tilts approaching 27°. However, with the optic axis at a nadir angle of 27°, it is reasonable to expect that slopes with tilts in the range 0-15° can be handled. For this bias angle and range of slopes, obscuration and multiple reflections do not appear to be significant. Even though the reflectance and the contrast will be larger at a bias angle of say 75°, (on the other side of the minimum in Figure 2-5), problems arising from obscuration and multiple reflections argue against that choice.

The field-of-view over which the reconstruction is feasible is limited by several factors. Evidently, for a large field-of-view, the nadir angle of the reflected ray will not be near 27° and the general considerations discussed above will be violated. In addition, corrections such as $\cos^4\zeta$ become important. Further, the transmission of optical systems are nonuniform over

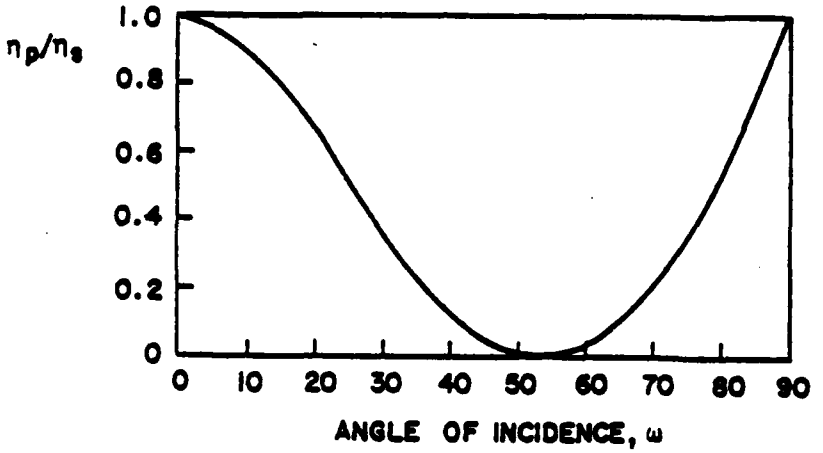

Figure 2-5 Determination of Angle of Incidence from the Ratio of the Reflectances $r_\eta = \eta_p/\eta_s$

large fields-of-view. Finally, the behavior of polarizers at angles far from normal incidence is unknown and could only degrade the results.

So far we had considered only the reflection of the light from the upper hemisphere. In reality, the light received from the surface contains in addition refracted upwelling radiation and Equation (2-6) should be modified as

$$H(\alpha,\beta) = \frac{\pi}{4F^2}\left[N(A,B)\eta(\omega) + N'(A',B')\frac{1-\eta(\omega)}{n^2}\right] \qquad (2.21)$$

where n is the refractive index of water and N'(A',B') is the upwelling radiance with incident direction specified by azimuth A' and polar angle B', and with the transmitted ray coincident with the refelcted ray. The angles (A,B), (A',B'), and ω are interrelated by Snell's laws. The value of N is typically ten times the value of N'. It is evident that the effect of the refracted light is to raise the average level of the received light and reduce the contrast in the image. These effects may be minimized by choosing to operate in a spectral range where upwelling radiation is relatively small. Since upwelling radiation has a spectral peak in the blue-green region, a red filter will substantially reduce the effects of upwelling radiation. A more detailed discussion can be found in an earlier report [8].

The success of the technique depends on the adequacy of reflected light within the chosen spectral region under normal outdoor illumination and the signal-to-noise ratios achievable with the chosen detector. These questions are examined fully in two earlier reports [7,9]. It appears that high speed infra red film has adequate sensitivity and that the reconstruction procedure is more tolerant of noise in the value of the slope tilt than the azimuth.

Since the light levels are already small, three separate cameras must be used so that light collection efficiency is not impaired. This separation necessarily results in errors due to parallax, i.e., the reflected rays (from the same location on the water surface) reaching the cameras are not identical. The necessity of three separate camera systems requires the identity of their optical characteristics, film characteristics and film processing. Further, since pixels in the three separate images corresponding

to the same surface location must be located for reconstruction, there must be on the surface at least three fiduciary marks so that such a registration of the three images can be accomplished (if internal registration is not feasible). The presence of the floats will cause some changes in the surface geometry and any errors in the image registration directly leads to errors in the slope values.

The moving surface of water contains structure down to millimeters (capillary waves) before surface tension precludes finer structure. The spatial resolution of the slope estimation is therefore of interest. A cursory examination may indicate that this would be determined by the camera and the detector (film and microdensitometer). In the present experiments, the microdensitometer aperture can be considered to set the limit. However, it should also be noted that an underlying assumption is that the reflected radiation averaged over the (detector) aperture is equal to the radiation reflected by the average slope. Further, the movement of the water surface during the exposure period is also averaged over the (detector) aperture. For these reasons, it is necessary that the these cameras be exposed simultaneously and for equal periods of exposure, which should be as short as possible. Our experience with the method is not adequate to estimate quantitatively the errors introduced by these sources. Some of the foregoing limitations can be removed by the use of electronic recording of the images.

3. THE EXPERIMENTS AT NORDA

The experiments were conducted at the outdoor wave basin at the NORDA facility in Bay St. Louis, MS shown in Figure 3-1. Dr. M-Y Su of NORDA has been using the wave basin to study non-linear wave dynamics for some time, by mechanically generating the waves (see Figure 3-2), and following their development through their various stages using capacitance-type wave staffs. This instrumentation is severely limited in providing data on the structure of the capillary region of the wave spectrum both by the inherent resolution and by the assumptions and computations necessary to convert temporal spectra to spatial spectra. It would be desirable to determine the latter by a direct method and remotely, if possible.

Dr. P.M. Smith, also of NORDA, has been investigating microwave emissions from the random wave surface in an attempt to validate various models and to separate the contributions to the emissivity of the surface due to capillaries related to wave instabilities from those directly induced by the wind. Drs. Daniel Kwoh and Bruce Lake of TRW have been studying radar backscatter from the water surface as a function of wind. The interpretation of their results will be significantly simplified if the capillary wave structure over different regions of the mechanically generated wave-field can be characterized. The optical measurements of wave slopes will provide data that will be useful to all these researchers and will also serve to establish a unique new way to provide sea surface truth for various applications.

Four identical Nikon F2A SLR 35 mm-cameras with Nikkor 50mm f/1.4 lenses and MD-3 motor drives were chosen to record the four photographs. The motor drives could be triggered simultaneously, from a single remote switch. Red filters (Kodak Wratten Number 25) and polarizers were used in front of the lenses. The red filters were used to block most of the upwelling radiation dominant below 600 nm. The pass directions of the polarizers were oriented at 0, 45, 90 and -45° to the horizontal. Kodak Highspeed Infrared film 2481 with high sensitivity in the 600-900 nm range was used to record the images.

The cameras were attached to an aluminum frame with their optic axes as close as possible (to minimize parallax errors). This required the rotation

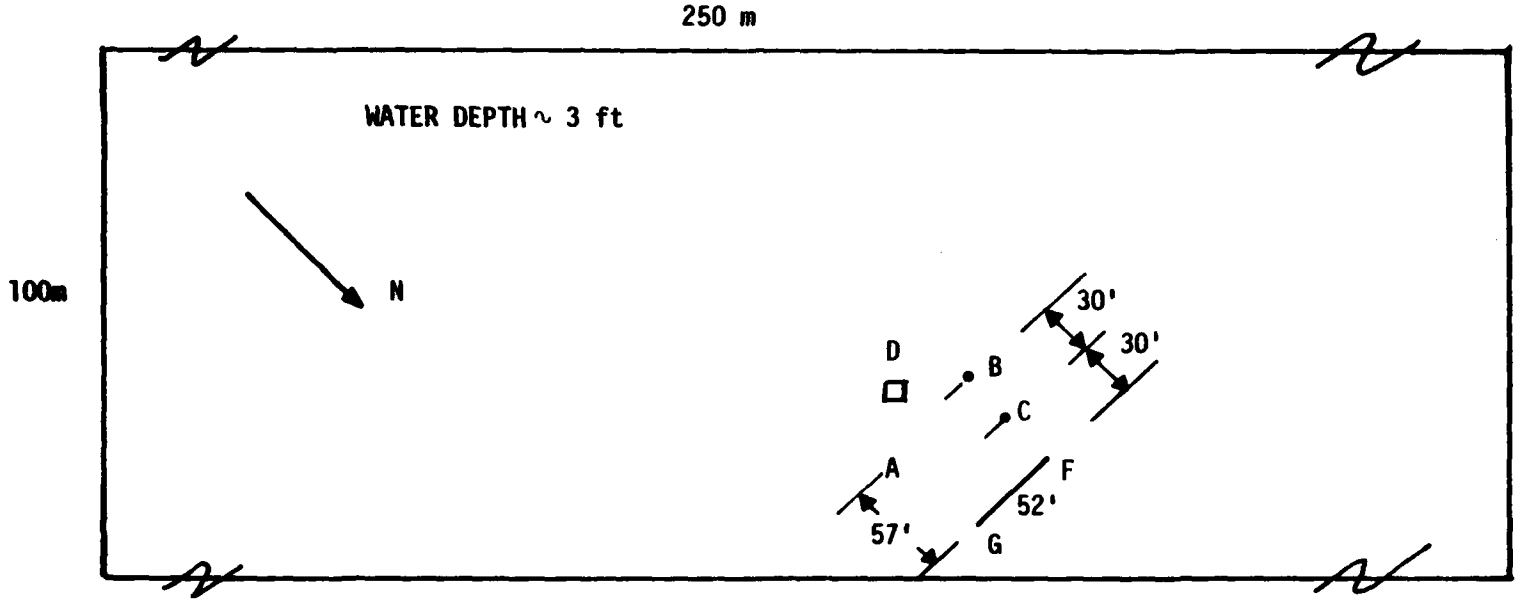

A - Camera Tower
B,C - Instrument Towers
F,G - Wave Maker
H - TRW Platform

Figure 3-1 Outdoor Wave Basin at NORDA Facility

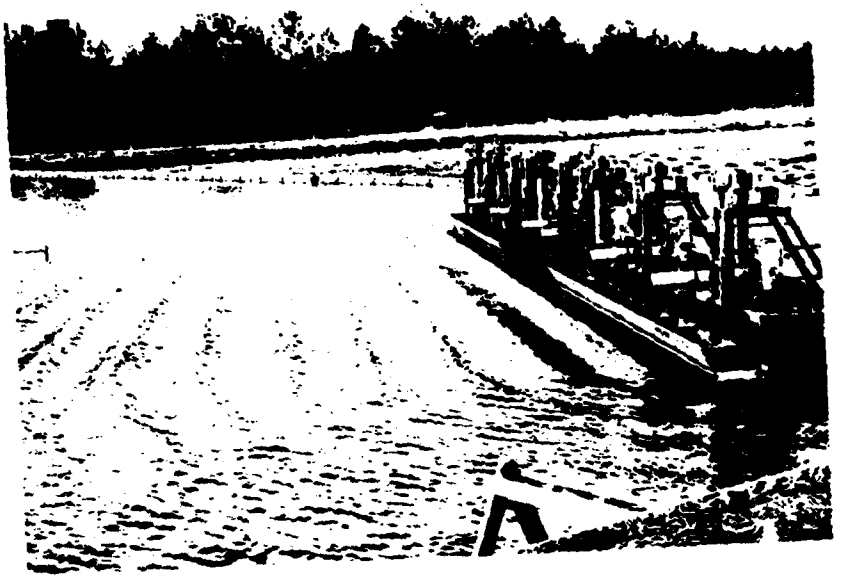

Figure 3-2 Wave Field Generated by Wave Maker in the Basin

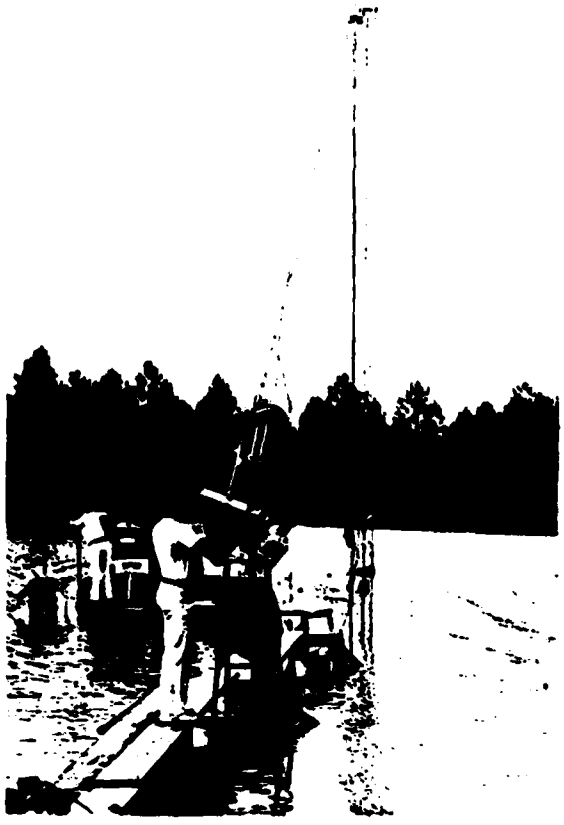

Figure 3-3 Tower Shown Lowered to Load Cameras

Figure 3-4 Tower Shown Raised During Experiments

of two of the cameras so that the rectangular image area of these two cameras were oriented at 90° to the other two. The aluminum frame was attached to a rotatable mount on an antenna tower which was hoisted erect after alignment of the cameras (Figures 3-3 and 3-4). A television camera boresighted with the Nikon cameras enabled control of the field-of-view of the cameras from a height of 70 ft above the water, with the nadir angle of their optic axes at about 30°.

A plan view of the experiment is shown in Figure 3-5. Four floats were secured to the bottom (1 meter depth) to appear near the corners of the FOV. Three of these are needed for registering the independent images and the fourth to check the accuracy of the registration. Four clearly resolved fixed objects whose positions are accurately known were also in the FOV. These are required to calculate and check the geometry of the optical systems. To provide a calibration of the exposure, several gray cards and a glass plate were included in the FOV. To check the simultaneity of the exposure of the cameras a rapidly rotating sector wheel was also used.

A large number of experiments were done. Due to the exploratory nature of these experiments, relatively calm wind conditions and an overcast unpolarized sky conditions were sought. A variety of mechanical waves were photographed. In addition, photographs were also acquired with Pan X and Plus X films with the water heavily dyed to suppress upwelling radiation. A list of the available films appears in Table 3.1.

Subsequent to the experiments, the Hurter-Driffield characteristic curves for the films used in the experiments were generated by exposing strips of the same batch of films through a calibrated step tablet and appropriate filters to unpolarized and diffused solar radiation. A schematic diagram of the apparatus used is shown in Figure 3-6. A calibrated detector and an oscilloscope were used to measure the energy density deposited on the films during these exposures. The four rolls of films from each of the experiments and several calibration strips from the same emulsion were processed simultaneously by hand.

The processed films were digitized using an Optronics International P-1000 microdensitometer. The H-D films were used to convert photographic

1- Frame Counter Lamps
2- Grey Conditions
3- Ground Glass Plate
4- Glass Plate
5- Sector Wheel
6- Floats

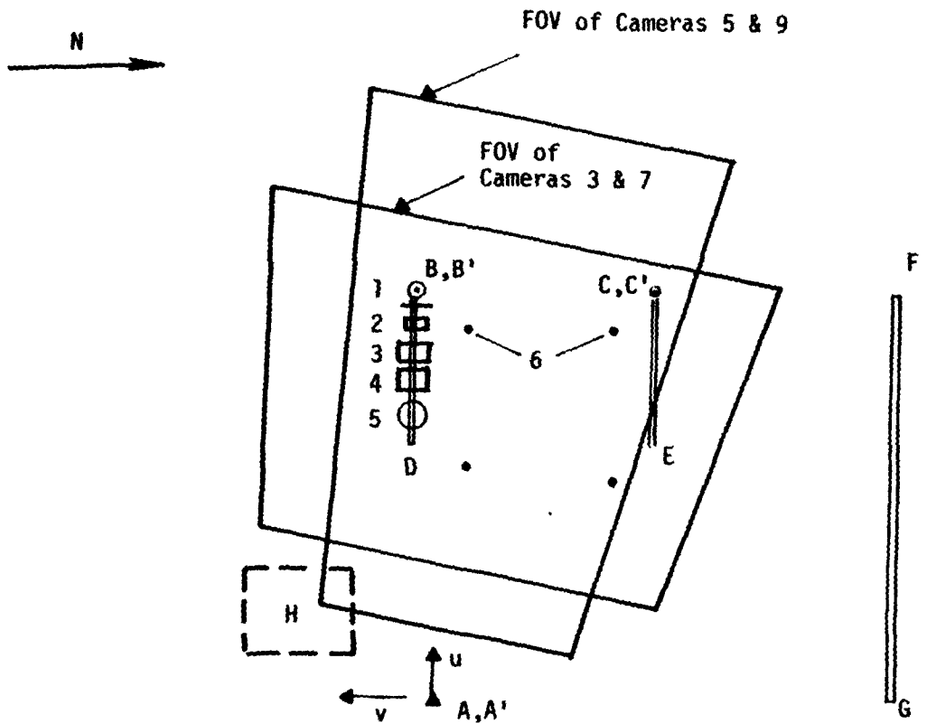

$\alpha = -12^{o}, \beta = 20^{o}$

		Coordinates, ft. u	v	w
A	Tower Base	0	0	0
A'	Cameras	0	0	70'
B(B')	Instrument Tower 1	52	3	0
C(C')	Instrument Tower 2	52	-27	0
D	End of Boom 1	32	3	7
E	End of Boom 2	32	-27	7
F	Wave Maker	0	-57	0
G	Wave Maker	52	-57	0

Figure 3-5 Plan View of the Experimental Setup

Table 3.1 Details of Wave Photographs Acquired and Available for Future Study

Expt. No.	Date	Time	Film Used	Red Filter Used	Water Conditions	Dye in Water	Sky Conditions	Video Tape	Quality Comments	Available Sets of Frames
5	11-02-81	1352	IR		GW SZ/P11		Unpolarized nonuniform	Yes	Good; dark	14-GW
6		1438	IR		WW-rough GW S2/P12		Unpolarized nonuniform		Good; dark	8-WW;5-GW
7		1531	IR		WW-calm GW-S2/P11		Unpolarized Nonuniform	Yes	Good; light	5-WW; 12-GW --
8		1620	PLUSX				Unpolarized nonuniform		Underexposed	--
9	11-03-81	1020	PLUSX		WW-calm GW S2/P13		Unpolarized nonuniform		Good	18-WW; 17-GW
10		1117	PLUSX	No	WW-calm GW-S2/P13	Yes	Unpolarized Cloudy		Good	15-WW; 16-GW
11		1539	PLUSX	No	WW-Calm GW-S2/P11					21-WW; 12-6W
14		0755	IR		WW-calm GW-S2/P11; S2/P12		Unpolarized Cloudy	Yes	Good	6-WW; 14-GW
15		0850	PanX	No	WW-calm GW-S2/P11; P12; S2/P13		Unpolarized Cloudy	Yes	Good	7-WW; 26-GW
16		1003	PanX	No	WW-calm GW-S2/P11; P12; S2/P13		Unpolarized Cloudy	Yes	Good	1-WW; 22-GW

W.W. = wind waves
M.W. = generated waves

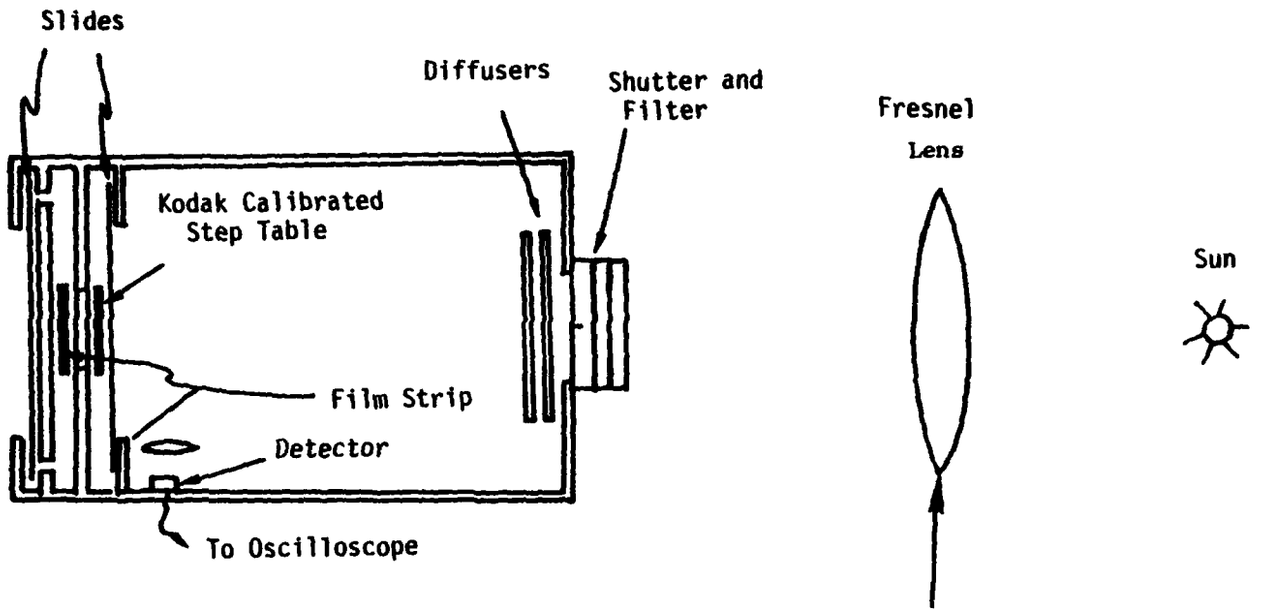

Figure 3-6: Schematic Diagram of Apparatus for Exposing Film Strips to Prepare H-D Curves

density values to energy density. The latter were used in subsequent processing.

The calibration filmstrips were also scanned and this measured density was related to the energy density using the data from the detector output to construct the H-D curves for each film strip. The average of several of these curves was used in further data processing.

4. ANALYSIS PROCEDURE

The digital processing of the polarized wave imges can be separated into the following stages:

(a) The microdensitometer provides an 8-bit digitization of the photograhic density averaged over a square aperture on a square grid of sampling positions. The aperture and the sampling grid are independently selectable.

(b) The scanned images are displayed and the coordinates of the floats are determined in each of the polarized images. These are used to calculate the translation, rotation, and scaling needed to superimpose three of the floats in two of the images onto the third (arbitrary) reference image. The registration accuracy may be checked with the remaining float. Using linear interpolation, the density values of the two superimposed images are calculated at positive corresponding to the pixel coordinates of the reference image, thus generating a triplet of density values corresponding to each sampled surface location.

(c) The data from the Hurter-Dreffield curve is now used to convert the photograhic density values into energy density values. Using the data from the grey card (unpolarized scatterer) images, corrections are made for the exposure differences. These may also be checked against the images of the glass plate (polarizing dielectric reflector).

(d) From measurements of the tower height, the distances between several fixed objects in the FOV and the focal length of the camera, the experimental geometry is reconstructed so that the correct azimuth and nadir angles (α,β) of the reflected ray corresponding to each pixel may be calculated. Checks of these computations against other objects in the FOV are also done at this stage.

(e) Using the triplet of corrected energy densities and the reflected ray

geometry, the value of the tilt and azimuth of the surface normal at each pixel location may be calculated as outlined in Section 2.

(f) The reconstructed surface normal results may be used to calculate the polarized image of the fourth camera and several statistical results on the behavior of the two-dimensional distribution of the slopes. The latter indicate histograms of the azimuth and tilt of surface normal, the two components of the slope along and across the look azimuth and the two dimensional spatial power spectra of the two slope components.

5. DATA ANALYSIS

This section presents the images and amplitude statistics for data collected at Bay St. Louis, Mississipi on November 3, 1981 along with images of the sea-slope constructed from the images. Images from experiment 15 listed in Table 3.1 were used with mechanically generated waves and calm wind conditions. In addition the difference between the actual and constructed irradiance, which is a check on the accuracy of the reconstructed slopes (see Section 2) is also displayed.

Figures 5-1, 5-2, 5-3, and 5-4, Part a, are images of the irradiance at polarizations of 0°, 45°, 90°, and 135° respectively. Each figure has been created from photographs, taken as described in Section 3, digitized, calibrated, and registered. Part b of each figure is the histogram for the image irradiances.

Figure 5-5 is the image of irradiance at polarization angle 135° constructed as explained in Section 2., i.e.,

$$X_{0^0} + X_{90^0} - X_{45^0}$$

Part a is the image. Part b is the histogram.

Figure 5-6 is an image of the difference between the actual and the constructed irradiance image at 135° polarization angle. Part a is the image. Part b is the histogram. The amplitude of the error is approximately one fourth the image amplitude.

Figure 5-7 is an image of the surface slope angle μ, constructed from the images at polarization angles 0°, 45°, and 90°. (Figures 5-1, 5-2, and 5-3.) Part a is the image. Part b is the histogram with the angle measured in radiance. Figure 5-8 is an image of the surface slope angle ν, constructed from same images. Parts a and b are the image and Part c is the histogram.

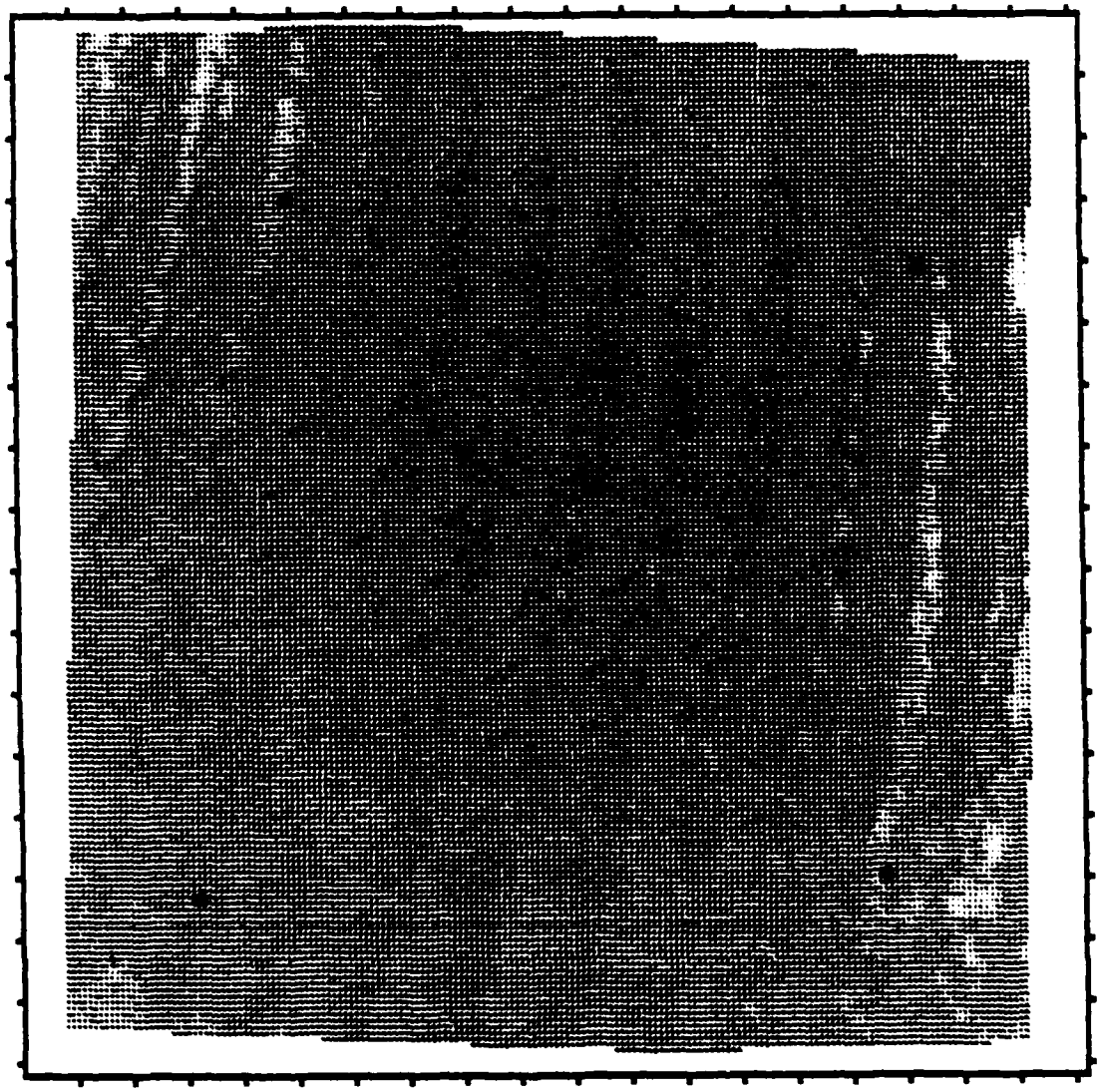

Figure 5-1a Irradiance at 0^{o} (Horizontal) Polarization Angle

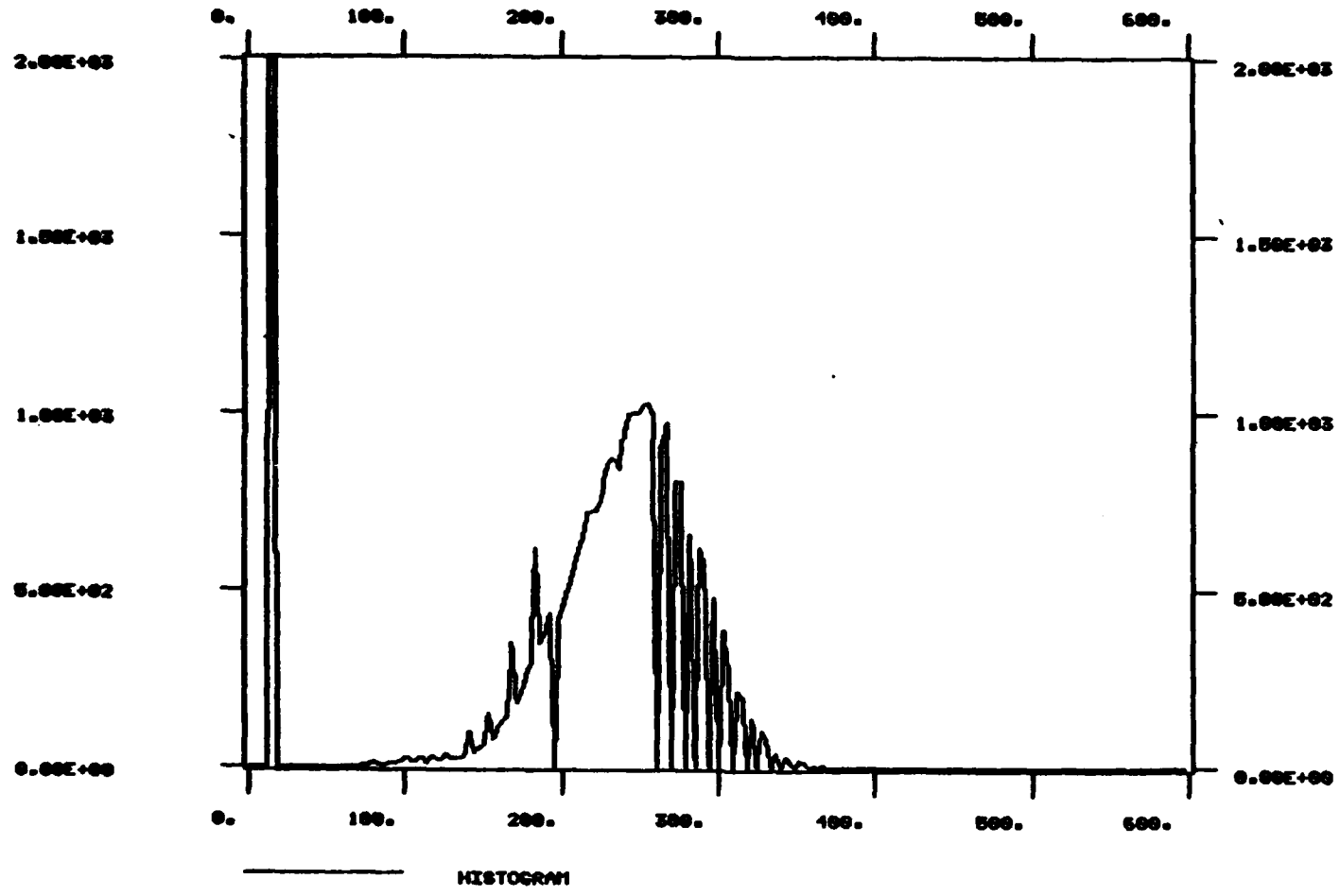

Figure 5-1b Histogram of Irradiance at 0^{o} Polarization Angle

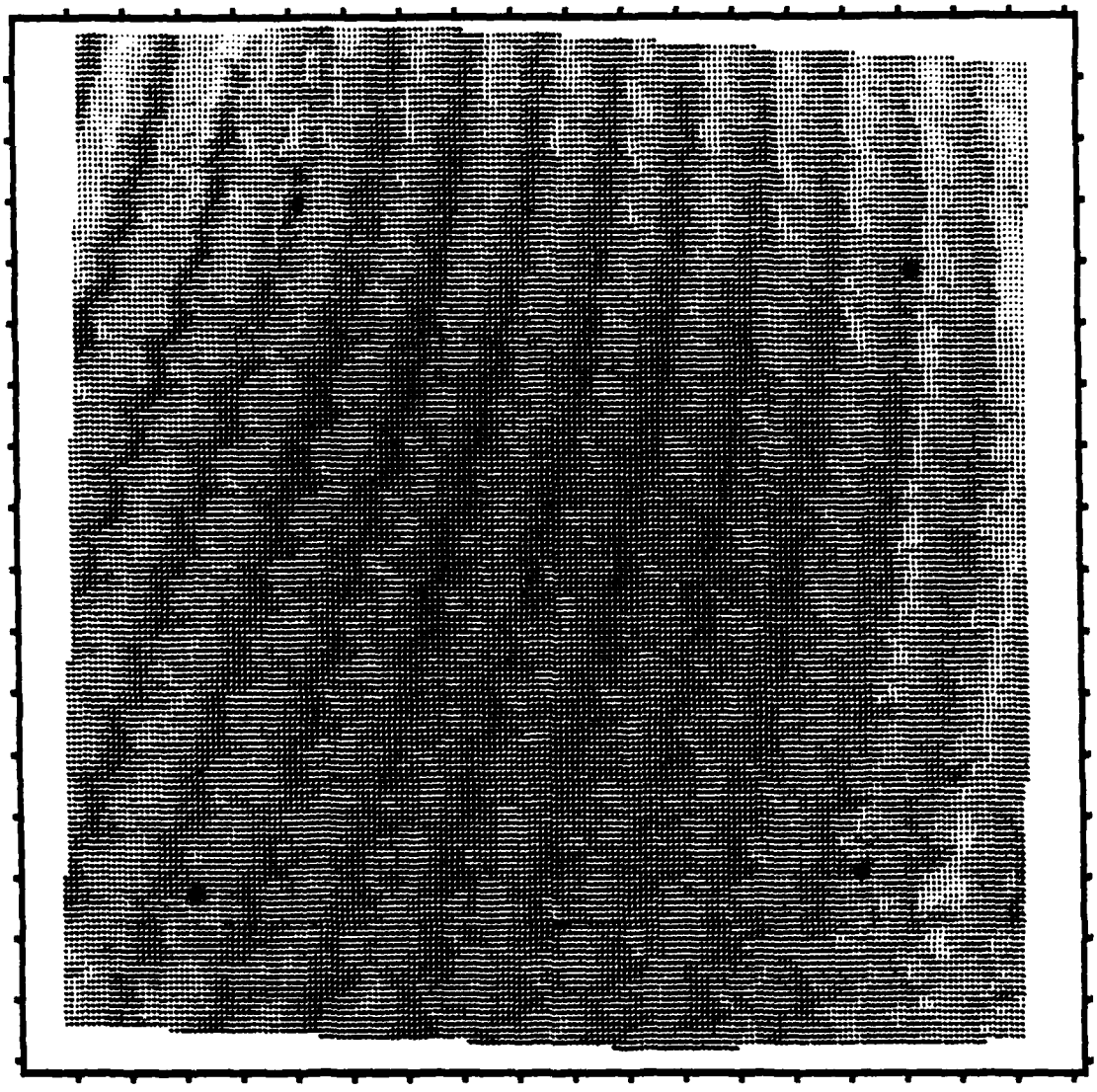

Figure 5-2a Irradiance at 45^{o} Polarization Angle

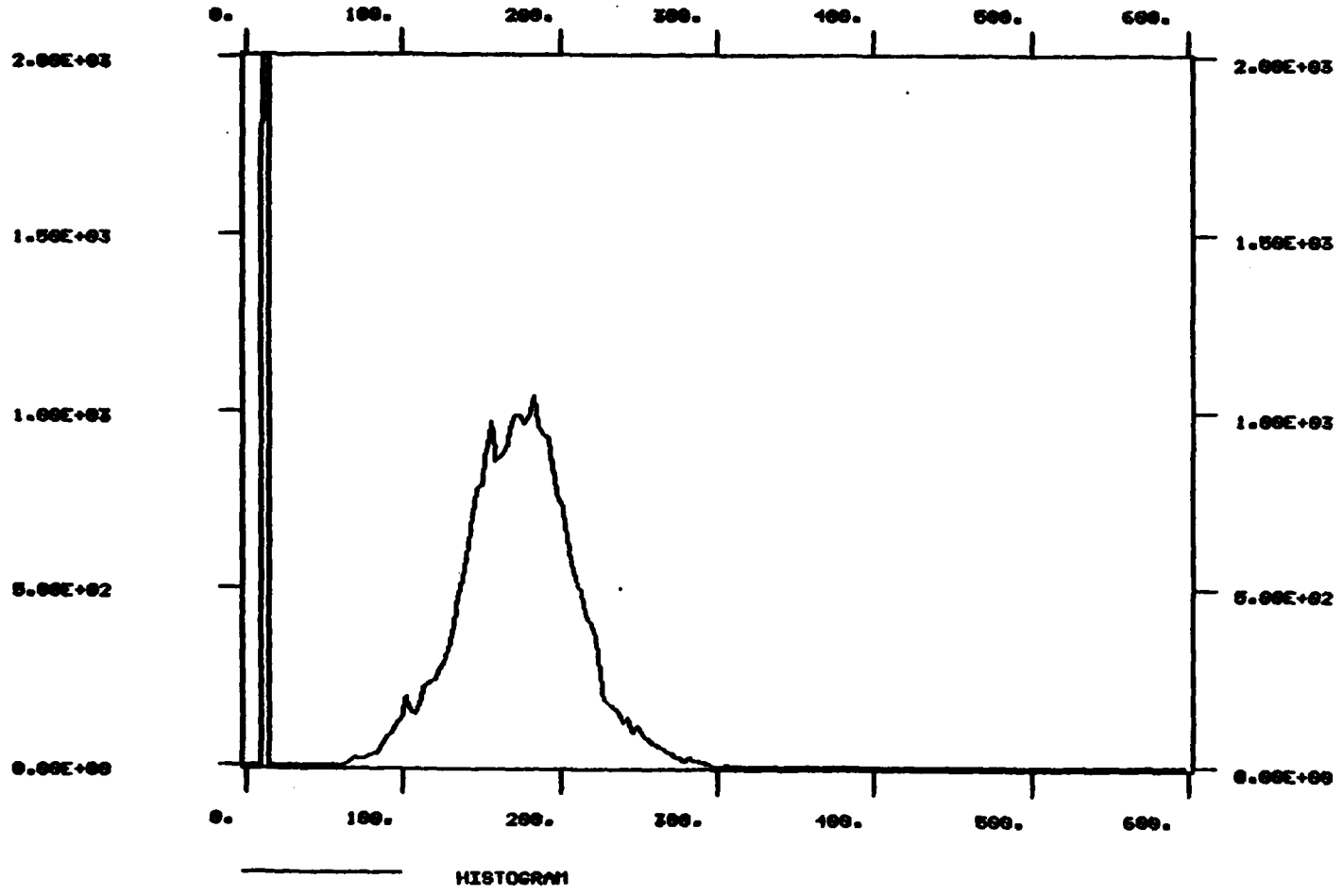

Figure 5-2b Histogram of Irradiance at 45° Polarization Angle

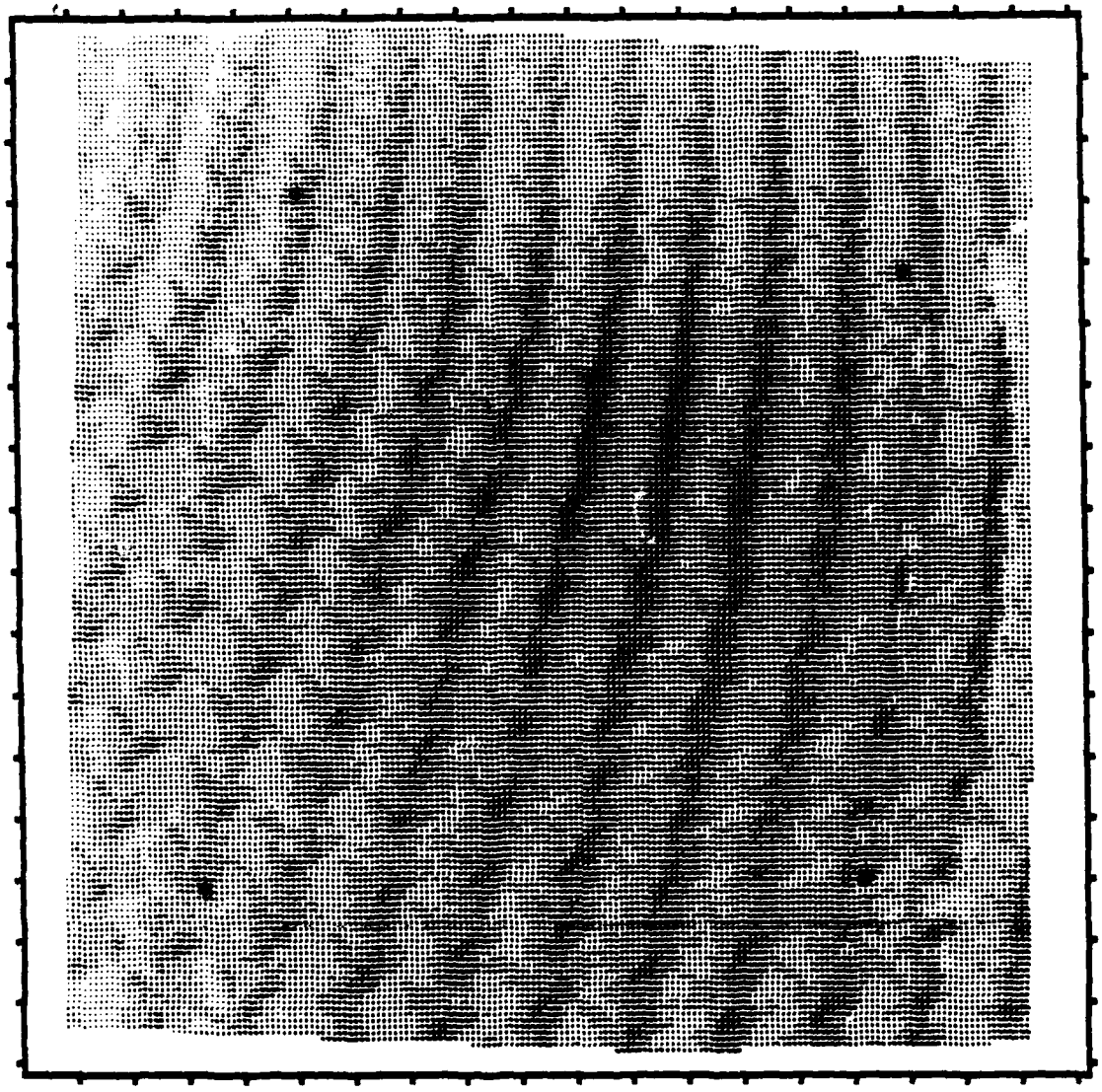

Figure 5-3a Irradiance at 90° (Vertical) Polarization Angle

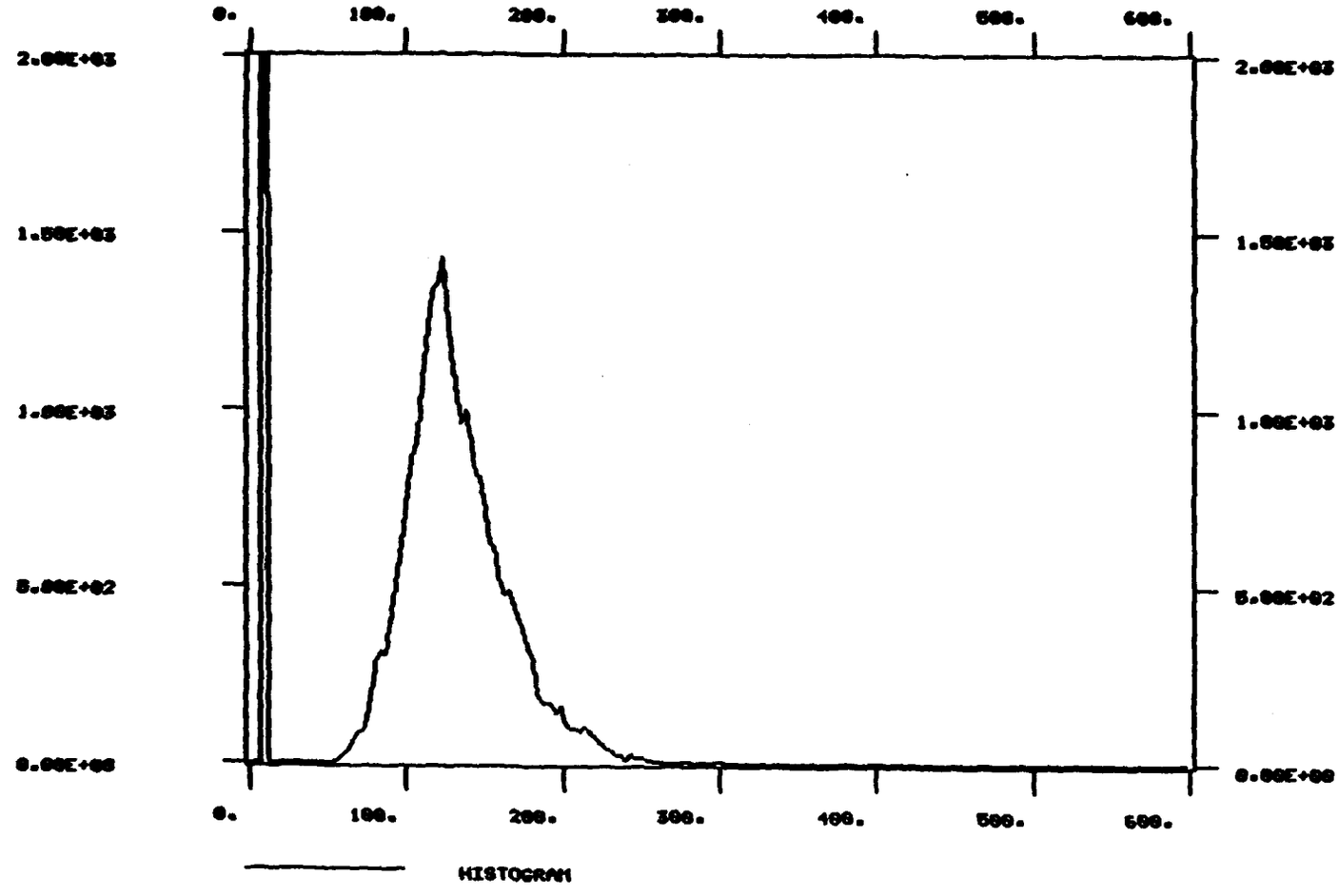

Figure 5-3b Histogram of Irradiance at 90° Polarization Angle

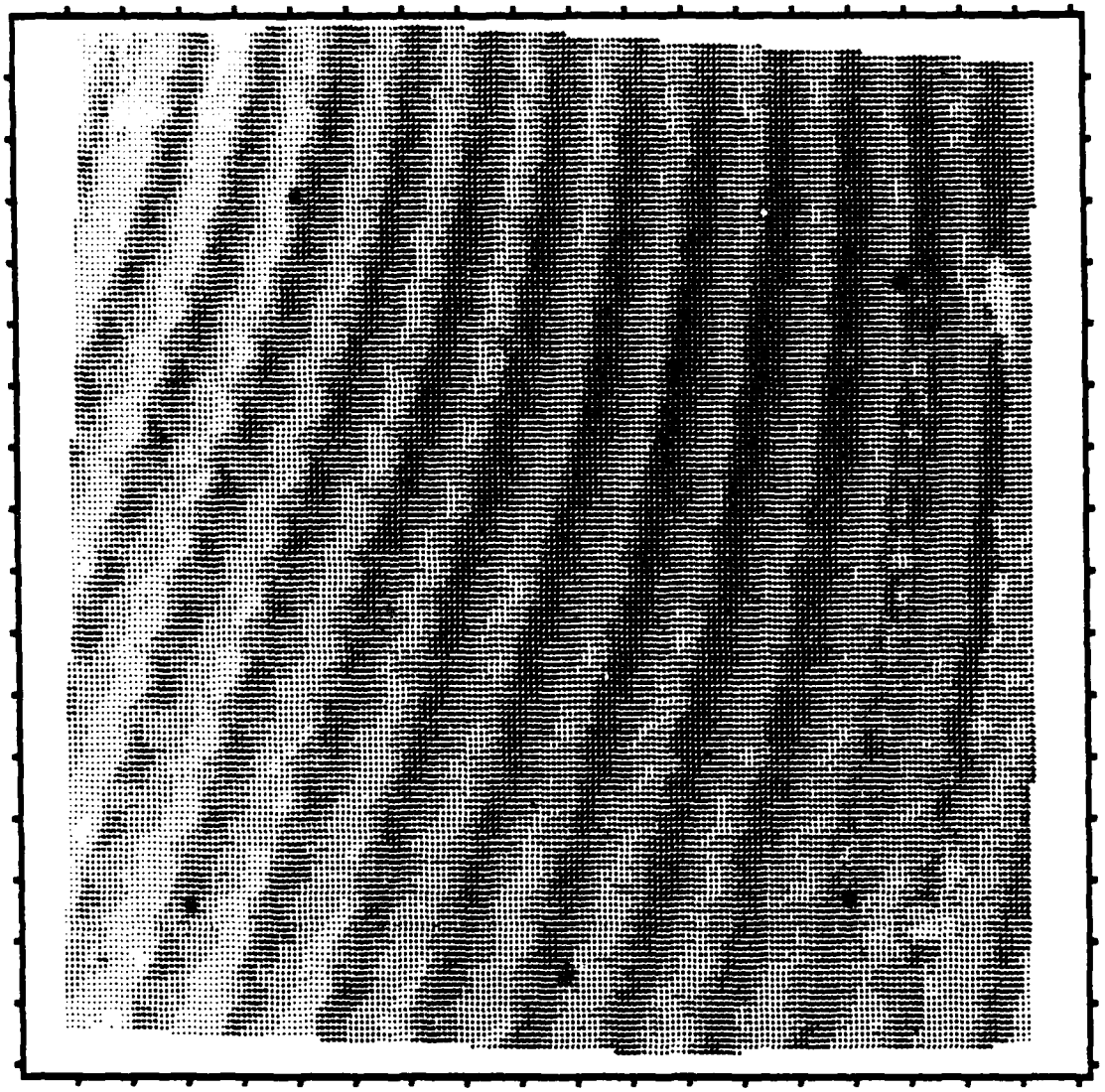

Figure 5-4a Irradiance at 135^{o} Polarization Angle

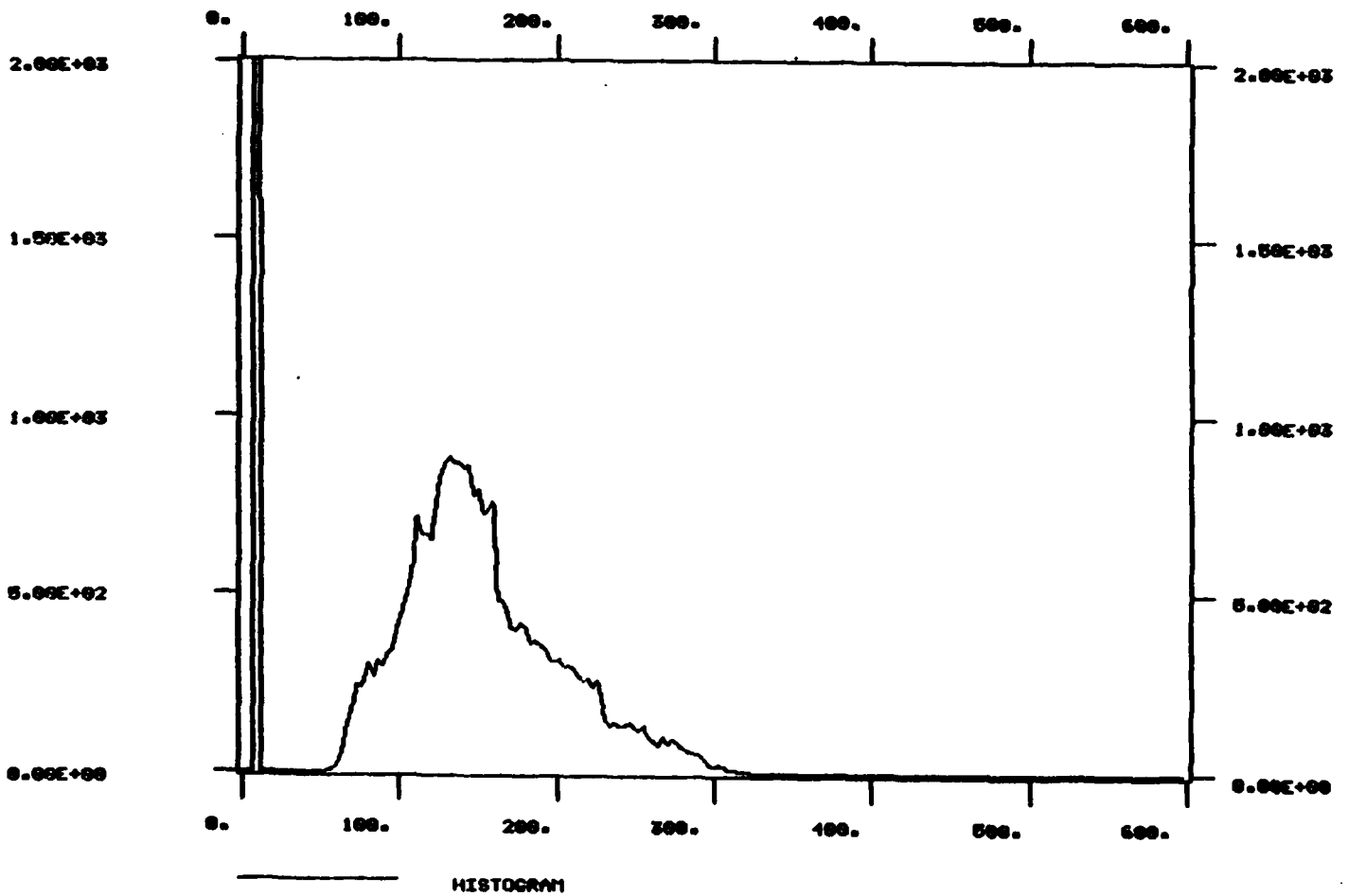

Figure 5-4b Histogram of Irradiance at 135° Polarization Angle

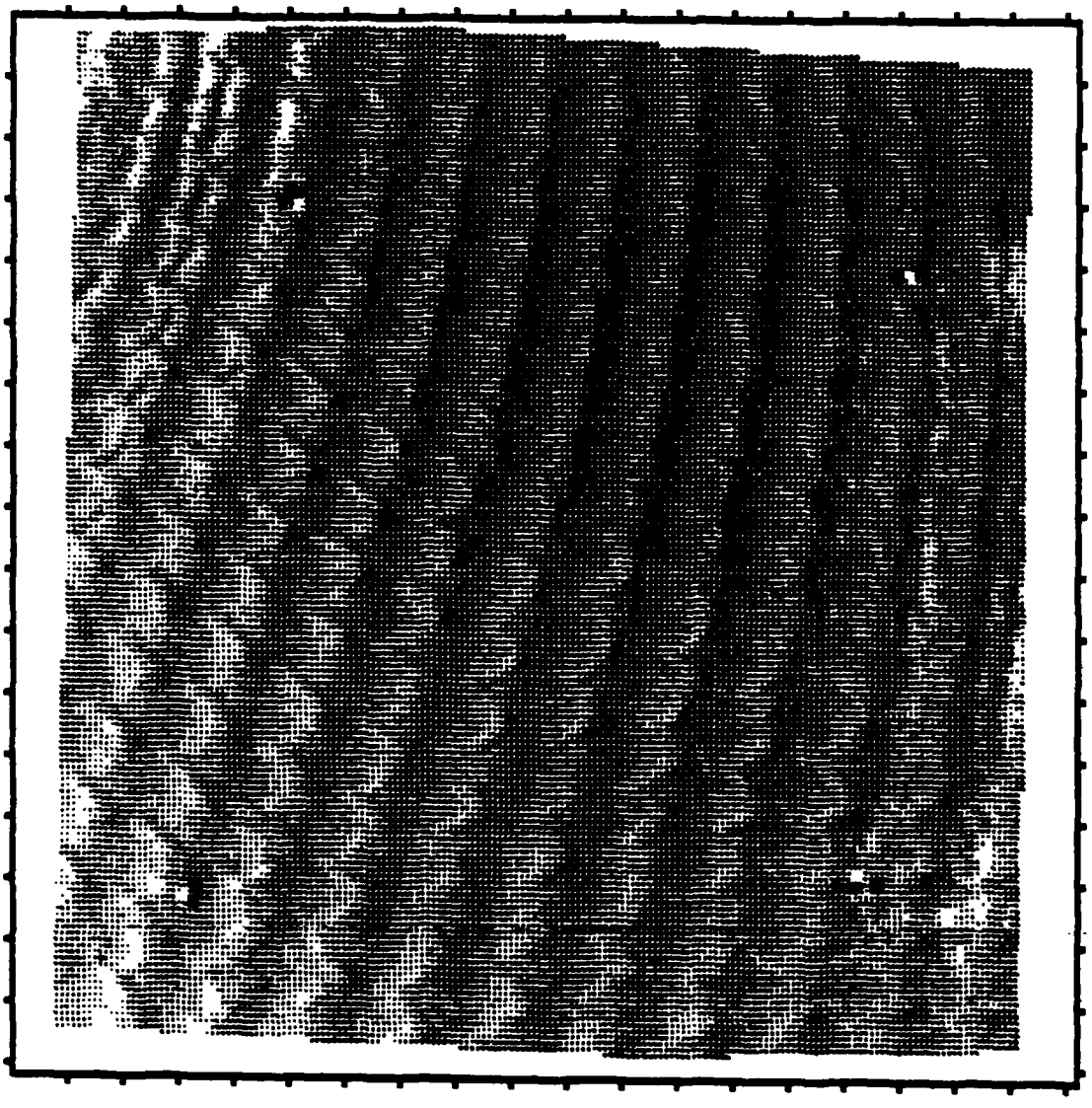

Figure 5-5a Constructed Irradiance at 135^{o} Polarization Angle

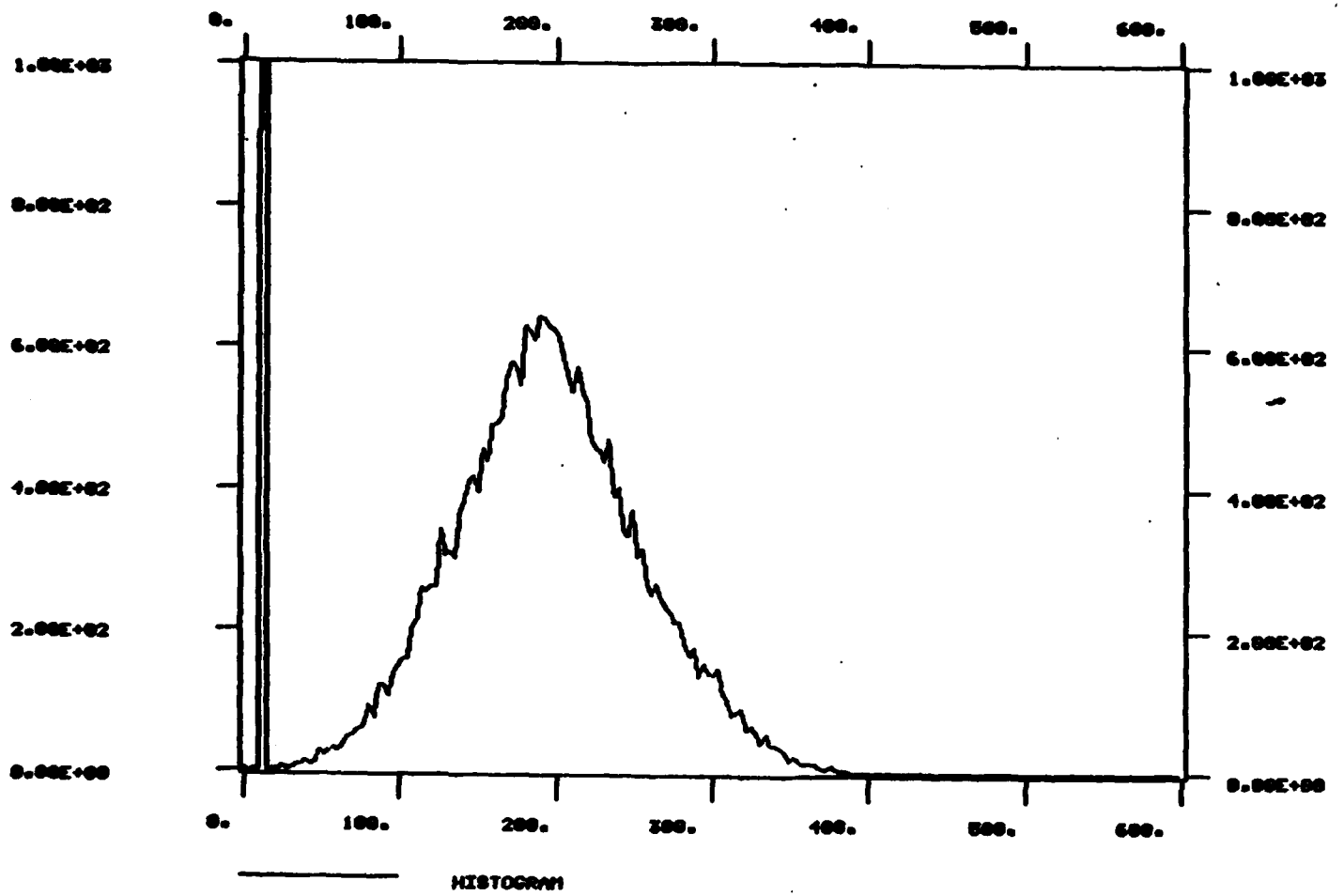

Figure 5-5b Histogram of Constructed Irradiance at 135° Polarization Angle

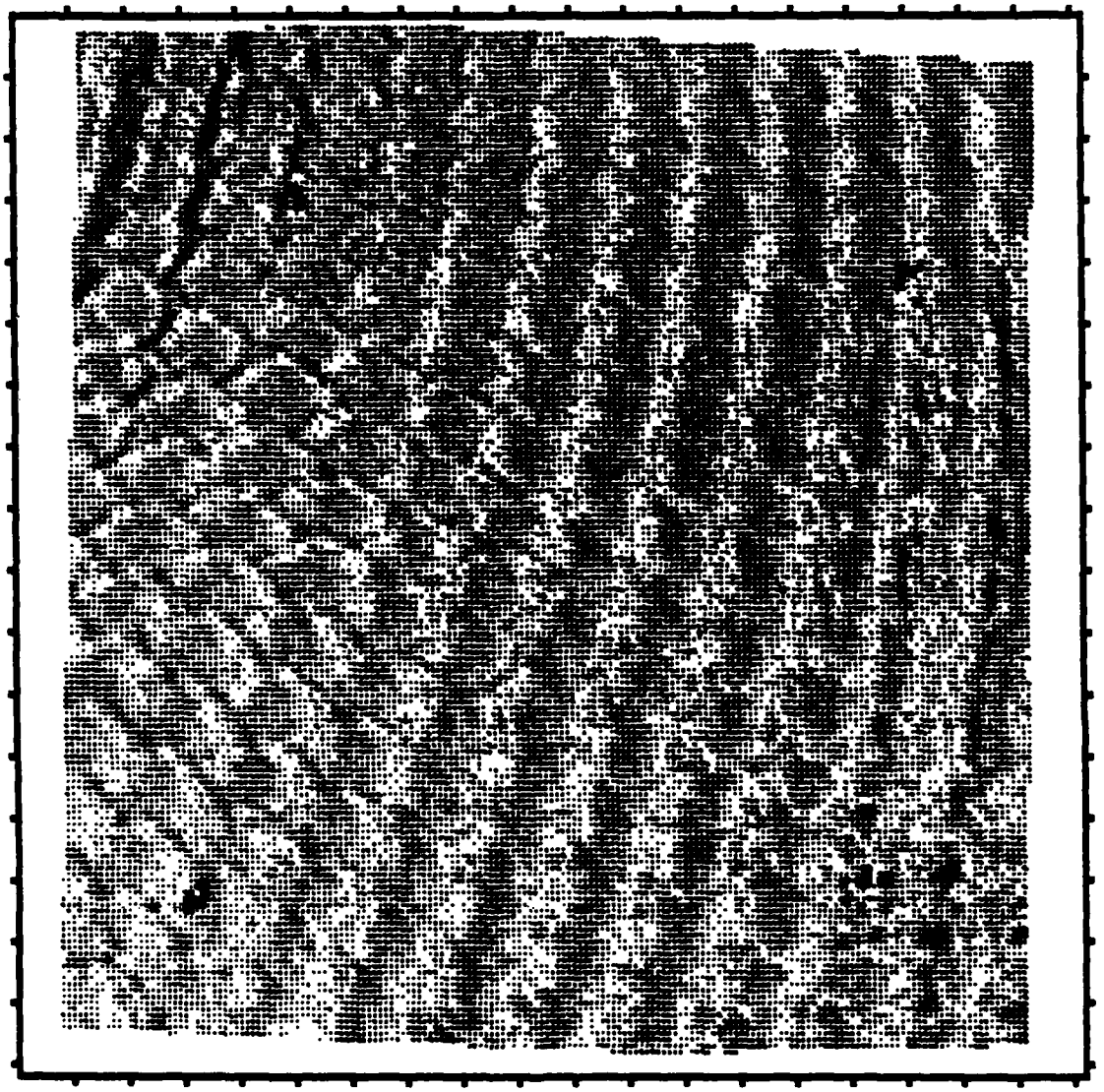

Figure 5-6a Irradiance Difference Magnitude

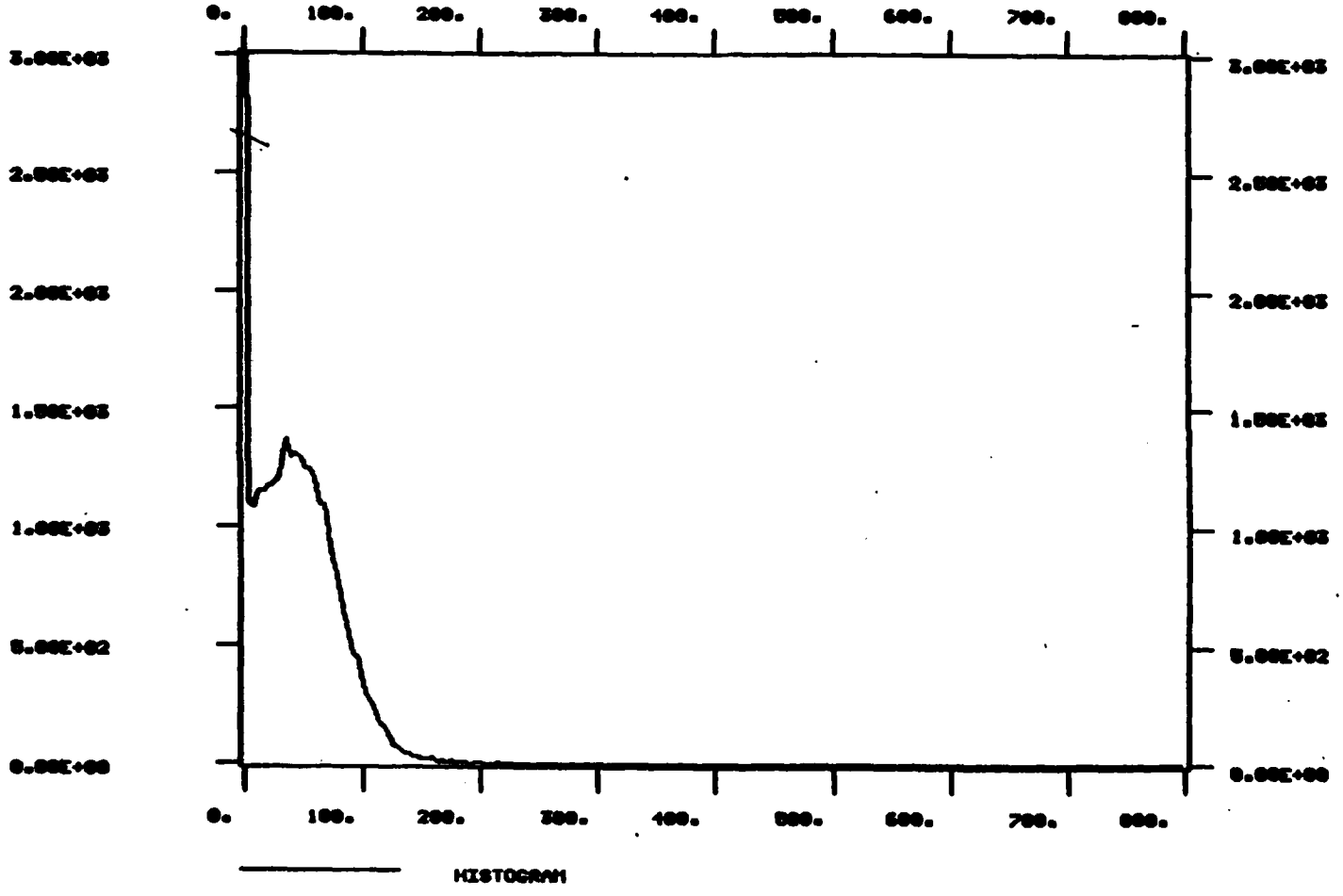

Figure 5-6b Histogram of Irradiance Difference Magnitude

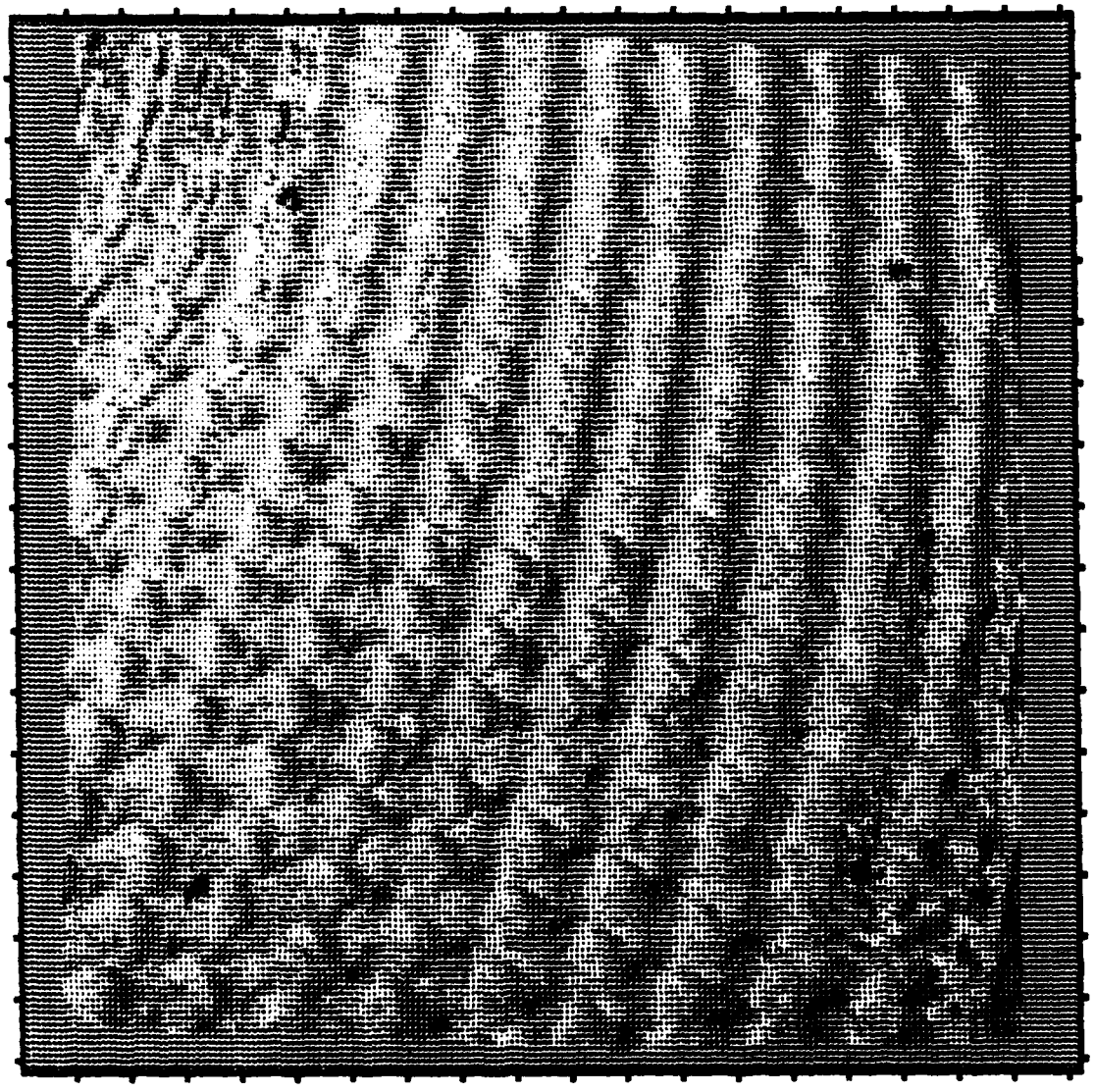

Figure 5-7a Constructed Surface Slope Angle μ

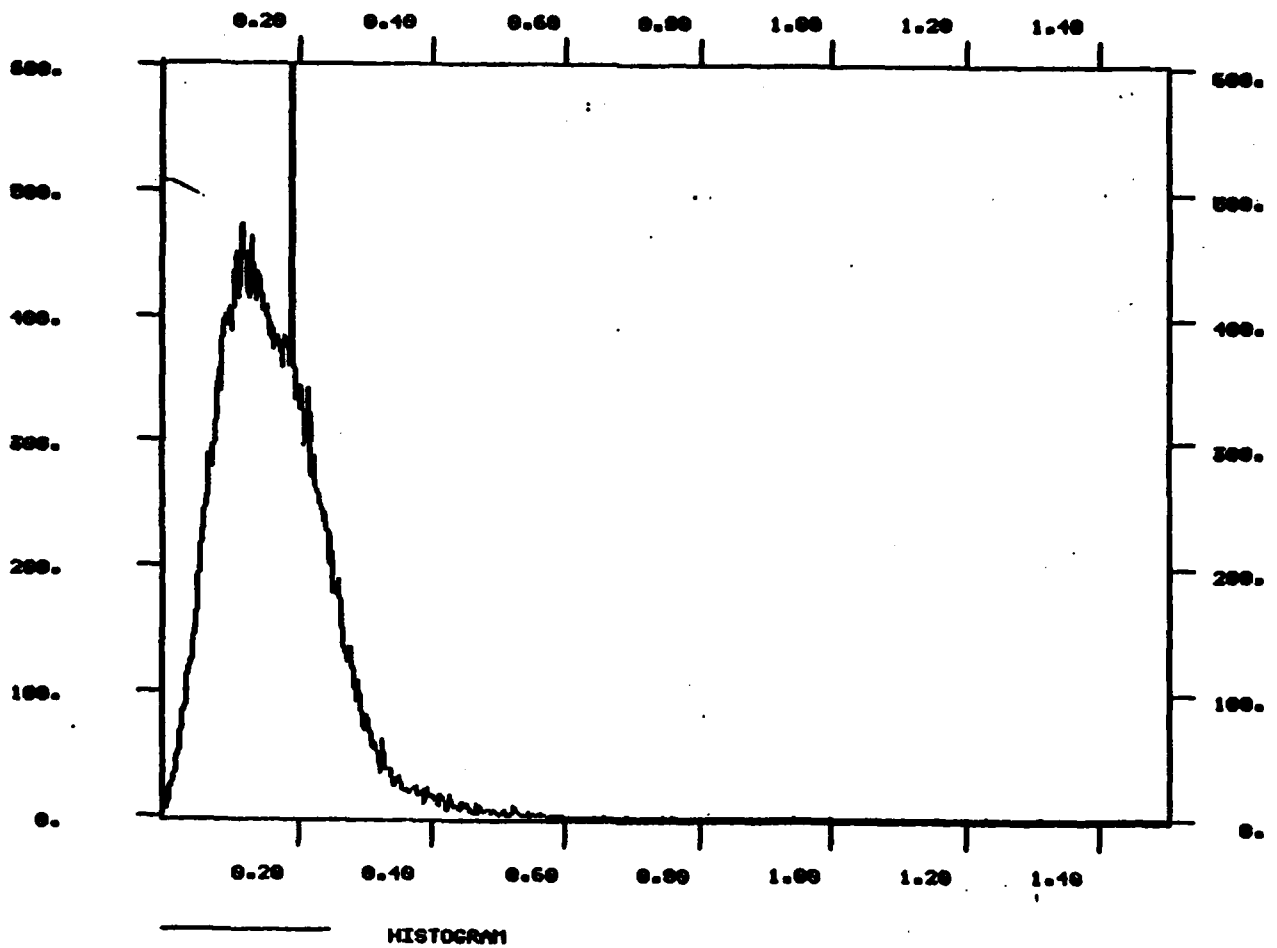

Figure 5-7b Histogram of Constructed Surface Slope Angle μ

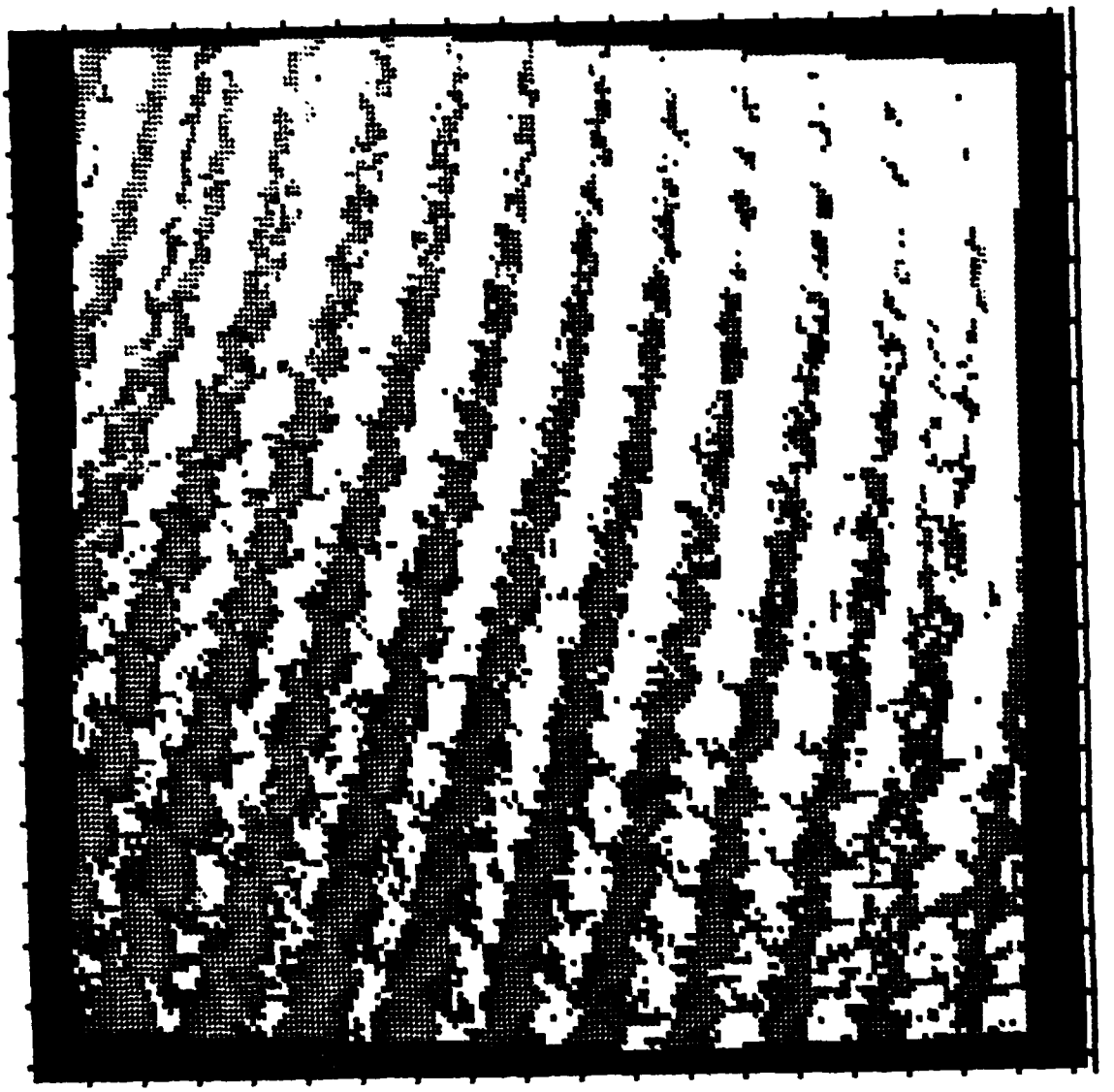

Figure 5-8a Constructed Sea Slope Angle ν

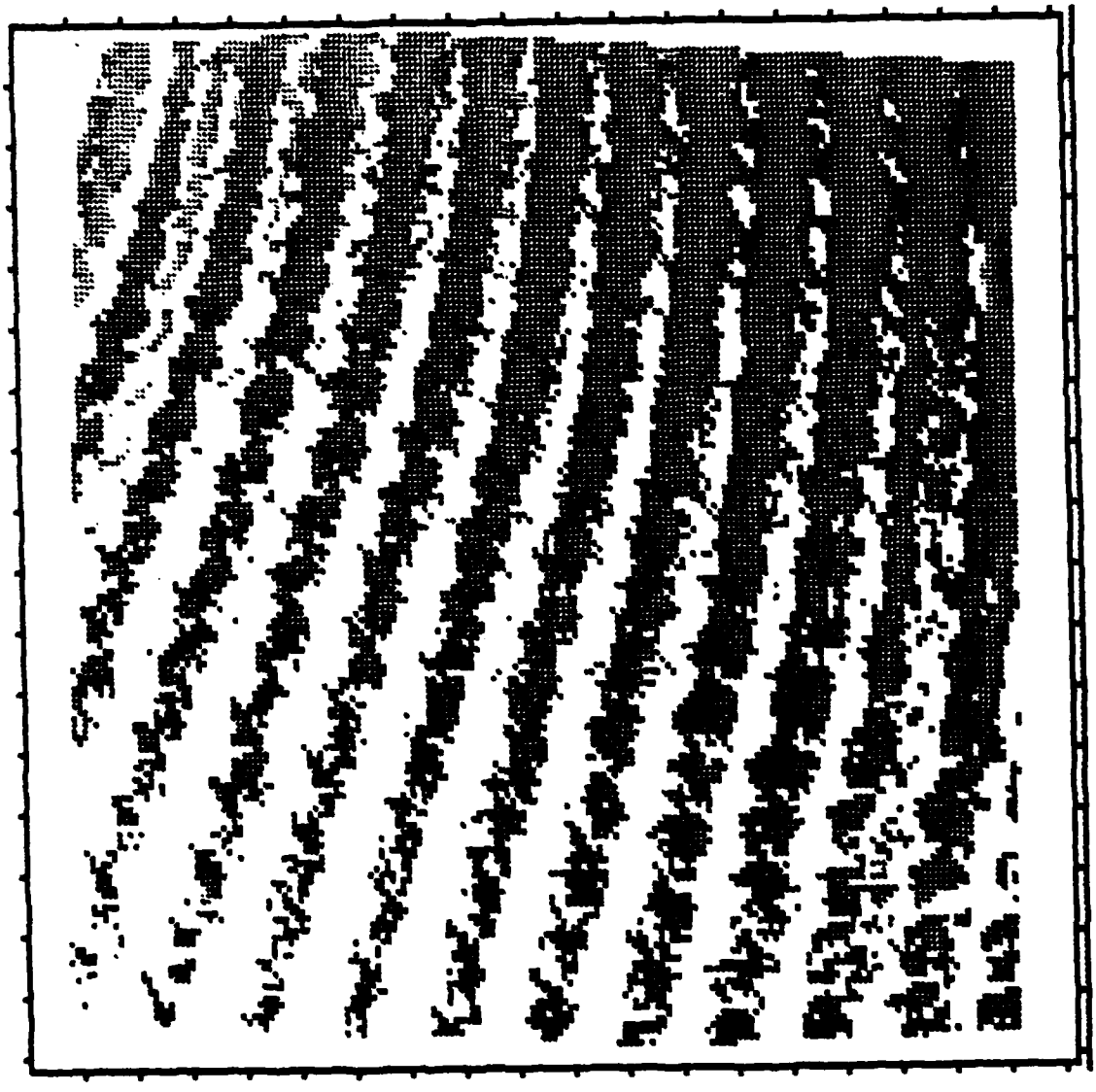

Figure 5-8b Constructed Sea Slope Angle ν (Negative Component)

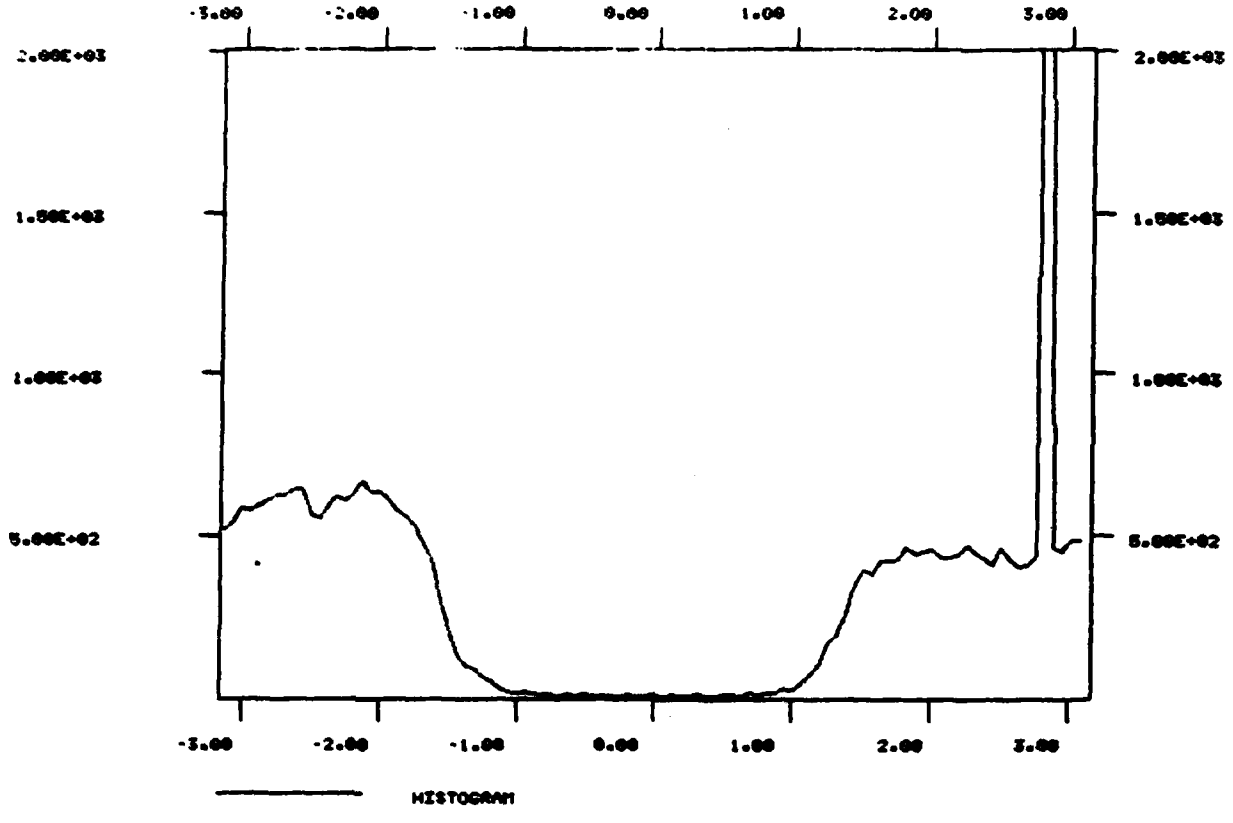

Figure 5-8c Histogram of Constructed Sea Slope Angle ν

6. REFERENCES

1. Cox, C. and W. H. Munk, "Measurement of the Roughness of the Sea Surface from Photographs of the Sun's Glitter," J. Opt. Soc. Am., Vol. 44, pp. 838-850 (1954).

2. Stilwell, D., Jr., "Directional Energy Spectra of the Sea from Photographs," J. Geophys. Res., Vol. 74, No. 8, p. 1974 (1969).

3. W. J. Pierson, Jr., and R. A. Stacy, "The Elevation Slope, and Curvature Spectra of a Wind Roughened Sea Surface," School of Engineering and Science, New York University, New York, NASA Contractor Report NASA CR-2247 (December 1973).

4. Cote, L. J. et al., "The Directional Spectrum of a Wind Generated Sea as Determined from Data Obtained by the Stero Wave Obsevation Project," New York University, New York, N.Y. (1960).

5. E. B. Dobson, "Measurement of the True Scale Structure of the Sea," J. Geophys. Res., Vol. 75, No. 15, p. 2854 (May 1970).

6. K. S. Krishnan and R. S. Poulsen, "Ocean Surface Simulation," Topical Report, Applied Physics Laboratory, The Johns Hopkins University, STD-R-372, Systems Control Technology, Palo Alto, CA, September 1980.

7. K. S. Krishnan, et al., "Reconstruction of Surface Slopes from Photographs of the Ocean," Proc. of SPCE Symposium on Ocean Optics VIII, Vol. 208, p. 206, (1979).

8. K. S. Krishnan, et al., "Comparative Evaluation of Ocean Surface Sensing Techniques," Annual Report APL/JHU POR-3695, Project 3818, SRI International, Menlo Park, California (April 1975) CONFIDENTIAL.

9. K. S. Krishnan and J. R. Jain, "Reconstruction of Surface Slopes from Photographs of the Ocean," Topical Report, Applied Physics Laboratory, The Johns Hopkins University, STD-R-409, Systems Control, Inc., Palo Alto, California, December 1980.